The Astrophysical Journal, 860:41 (22pp), 2018 June 10 https://doi.org/10.3847/1538-4357/aac514

The Spectral and Environment Properties of $z \sim 2.0$–2.5 Quasar Pairs

Elisabeta Lusso[1], Michele Fumagalli[1,2], Marc Rafelski[3,4], Marcel Neeleman[5,6], Jason X. Prochaska[5,7], Joseph F. Hennawi[6,8], John M. O'Meara[9], and Tom Theuns[2]
[1] Centre for Extragalactic Astronomy, Department of Physics, Durham University, South Road, Durham, DH1 3LE, UK; elisabeta.lusso@durham.ac.uk
[2] Institute for Computational Cosmology, Durham University, South Road, Durham DH1 3LE, UK
[3] Space Telescope Science Institute, 3700 San Martin Drive, Baltimore, MD 21218, USA
[4] Department of Physics & Astronomy, Johns Hopkins University, Baltimore, MD 21218, USA
[5] University of California Observatories, Lick Observatory, 1156 High Street, Santa Cruz, CA 95064, USA
[6] Max-Planck-Institut fuer Astronomie, Koenigstuhl 17, D-69117 Heidelberg, Germany
[7] Department of Astronomy and Astrophysics, University of California, 1156 High Street, Santa Cruz, CA 95064, USA
[8] Department of Physics, Broida Hall, University of California, Santa Barbara, CA 93106, USA
[9] Department of Physics, Saint Michael's College, One Winooski Park, Colchester, VT 05439, USA
Received 2018 February 23; revised 2018 May 4; accepted 2018 May 4; published 2018 June 11

Abstract

We present the first results from our survey of intervening and proximate Lyman limit systems (LLSs) at $z \sim 2.0$–2.5 using the Wide Field Camera 3 on board the *Hubble Space Telescope*. The quasars in our sample are projected pairs with proper transverse separations $R_\perp \leqslant 150$ kpc and line-of-sight velocity separations $\lesssim$11,000 km s^{-1}. We construct a stacked ultraviolet (rest-frame wavelengths 700–2000 Å) spectrum of pairs corrected for the intervening Lyman forest and Lyman continuum absorption. The observed spectral composite presents a moderate flux excess for the most prominent broad emission lines, a ∼30% decrease in flux at $\lambda = 800$–900 Å compared to a stack of brighter quasars not in pairs at similar redshifts, and lower values of the mean free path of the H I ionizing radiation for pairs ($\lambda_{\rm mfp}^{912} = 140.7 \pm 20.2\,h_{70}^{-1}$ Mpc) compared to single quasars ($\lambda_{\rm mfp}^{912} = 213.8 \pm 28\,h_{70}^{-1}$ Mpc) at the average redshift $z \simeq 2.44$. From the modeling of LLS absorption in these pairs, we find a higher (∼20%) incidence of proximate LLSs with $\log N_{\rm H\,I} \geqslant 17.2$ at $\delta v < 5000$ km s^{-1} compared to single quasars (∼6%). These two rates are different at the 5σ level. Moreover, we find that optically thick absorbers are equally shared between foreground and background quasars. Based on these pieces of evidence, we conclude that there is a moderate excess of gas-absorbing Lyman continuum photons in our closely projected quasar pairs compared to single quasars. We argue that this gas arises mostly within large-scale structures or partially neutral regions inside the dark matter halos where these close pairs reside.

Key words: accretion, accretion disks – galaxies: active – intergalactic medium – quasars: absorption lines – quasars: general

Supporting material: figure sets, machine-readable tables

1. Introduction

Quasars represent the brightest phase of the active galactic nuclei (AGNs) population, with optical–ultraviolet luminosities in the range $\sim 10^{44}$–10^{48} erg s^{-1}. To support these luminosities, a significant mass of gas must flow from kiloparsec scales to the center of the galaxy at subparsec scales. One possible mechanism to drive gas to the galaxy's center is through gas-rich major mergers (e.g., Di Matteo et al. 2005; Hopkins et al. 2005, 2006, 2008; Springel et al. 2005), but minor mergers (e.g., Corbin 2000) and secular processes (e.g., Cisternas et al. 2011) are also probable mechanisms for funneling gas toward the central supermassive black hole (SMBH). Models of structure formation can reproduce the observed large-scale quasar properties (e.g., clustering, environment measurements) if the bright and short-lived quasar phase within the galaxy lifetime is triggered by mergers (see Alexander & Hickox 2012 and references therein).

Pair[10] (or dual) quasars with (projected) separation at tens of megaparsecs to several hundreds of kiloparsecs have become particularly interesting in the last decade as these systems could reside in the same cosmological structure, thus tracing the large-scale quasar environment (e.g., Hennawi et al. 2006b, 2010; Sandrinelli et al. 2014, 2018; Eftekharzadeh et al. 2017). The detection of these systems in the optical and mid-infrared, mostly from the Sloan Digital Sky Survey (SDSS) and the *Wide-field Infrared Survey Explorer*, down to a few tens of kiloparsecs, reinforces the idea of gas-rich mergers mutually triggering the active nuclear phase likely in both quasars (e.g., Myers et al. 2008; Foreman et al. 2009; Satyapal et al. 2014, 2017; Weston et al. 2017). Quasar pairs at similar redshifts, with projected separations less than a few hundreds of kiloparsecs, are thus ideal probes of the large-scale environment, since this is where mergers are more likely to occur, thereby providing possible tracers of massive proto-clusters (e.g., Djorgovski et al. 2007; Liu et al. 2011; Farina et al. 2013; Deane et al. 2014; Hennawi et al. 2015).

In this paper, we further investigate the large-scale quasar environment by analyzing the spectral properties (e.g., ionizing continuum, emission line fluxes) and associated absorbers of quasar pairs with proper transverse separation $R_\perp \leqslant 150$ kpc and line-of-sight velocities $<$11,000 km s^{-1} in the redshift interval $z \simeq 2.0$–2.5. Our sample consists of 47 relatively close quasar pairs at similar redshifts observed during our survey for Lyman limit systems (LLSs, i.e., optically thick absorption-line systems) using the Wide Field Camera 3 on board the *Hubble*

[10] In the following, we will refer to a *pair* as a system of two quasars with small projected and spectroscopically confirmed redshift separations.

Space Telescope (*HST*; Proposal ID: 14127). Our survey also includes six lensed quasars, two field single quasars (SDSS J133905.25 + 374755.3 and SDSS J154815.42 + 284452.6), and a projected pair (i.e., the system SDSS J172855.24+ 263449.1 and SDSS J172855.31 + 263458.1 with line-of-sight velocity separations N11,000 km/s), which will be discussed in a separate paper, leading to a total of 104 single sources (111 observations). By comparing the ionizing spectral continuum of quasar pairs at $z > 2$ as a function of luminosity to similar quantities of single quasars at comparable redshifts, we can provide constraints on the structure of the intergalactic medium (IGM) at the 10–100 kpc scale (in the transverse direction) where these systems reside.

From modeling the associated absorbers (LLSs and damped Lyα systems, DLAs, with $\log N_{\rm H\,I} \geqslant 20.3$), we investigate the interplay between quasars and their environment, as well as constrain the evolution of the ultraviolet background. Quasars indeed provide significant flux of ionizing photons that regulate both the ionization state and the temperature of the IGM at $z \sim 3$ (e.g., Haardt & Madau 1996, 2012; Meiksin & White 2003; Faucher-Giguère et al. 2009). While not numerous enough at $z \gtrsim 6$ to have significantly contributed to the H I reionization (e.g., Meiksin 2005; Shankar & Mathur 2007; Jiang et al. 2008; Willott et al. 2010; Fontanot et al. 2012, 2014), they are the main sources responsible for the reionization of He II at $z \sim 3$ (Miralda-Escudé et al. 2000; Faucher-Giguère et al. 2008; Furlanetto 2009; McQuinn et al. 2009; Haardt & Madau 2012; Compostella et al. 2013). The common denominator of all these studies is that they rely upon the parameterizations of the quasar continuum at rest-frame UV wavelengths.

The composite spectrum of quasars also provides a wealth of additional information. Observationally, composite spectra of AGNs were previously constructed by taking advantage of major surveys, covering a relatively large range of redshifts: the Large Bright Quasar survey (Francis et al. 1991), Faint Images of the Radio Sky at Twenty-cm (FIRST; Brotherton et al. 2001), SDSS (Vanden Berk et al. 2001), *HST* (Zheng et al. 1997; Telfer et al. 2002; Shull et al. 2012; Stevans et al. 2014; Lusso et al. 2015; Tilton et al. 2016), and the *Far Ultraviolet Spectroscopic Explorer* (*FUSE*; Scott et al. 2004). The composites in these studies indicate that the optical continuum can be described by a power law of the form $f_\nu \propto \nu^{\alpha_\nu}$, with a slope spanning a rather wide range of values (e.g., $-0.83 \lesssim \alpha_\nu \lesssim -0.61$ in the rest-frame wavelength range 1200–2000 Å; Telfer et al. 2002; Shull et al. 2012; Stevans et al. 2014; Lusso et al. 2015).

The quasar composites also show a softening in the far ultraviolet (blueward of Lyα), which is interpreted as comptonization of the thermal disk emission in a soft X-ray corona above the disk (Czerny & Elvis 1987; Laor et al. 1997; Zheng et al. 1997). However, Scott et al. (2004, S04 hereafter), who considered more than 100 AGNs at $z < 0.1$ observed with *FUSE*, found that the quasar composite does not display any break or softening of the continuum, but a significantly hard slope with $\alpha_\nu = -0.56$ at the rest-frame wavelength range 630–1100 Å. Stevans et al. (2014) investigated possible reasons for this difference (see their Figures 7 and 8), concluding that the *FUSE* spectral stack was affected by quasar broad emission lines in the wavelength range covered by *FUSE*. Additionally, the *FUSE* survey considered low-redshift quasars, and the rest-frame wavelengths longer than 1100 Å were not covered.

The observed quasar spectra can also be used to trace the evolution of the ionization state of the IGM through the estimate of the effective opacity in the Lyman continuum ($\tau_{\lambda,\rm eff}$), which is often represented by the mean free path, $\lambda_{\rm mfp}^{912}$. The $\lambda_{\rm mfp}^{912}$ parameter is defined as the physical distance a packet of ionizing photons can travel before encountering an e^{-1} attenuation (e.g., Worseck et al. 2014). As such, the $\lambda_{\rm mfp}^{912}$ should approach zero as the redshift increases toward the epoch of reionization. The redshift evolution of the $\lambda_{\rm mfp}^{912}$ is thus a key cosmological parameter that constrains the distribution of neutral hydrogen in the universe, while the estimate of the attenuation $\tau_{\lambda,\rm eff}$ ($\propto 1/\lambda_{\rm mfp}^{912}$; Prochaska et al. 2009) is a key parameter in constraining the extragalactic UV background (e.g., Madau & Haardt 2015, and references therein). Direct estimates of the mean free path have been obtained through the analysis of composite quasar spectra in the rest frame at $z \gtrsim 4.4$ using high signal-to-noise ratio (S/N) and low-resolution spectra taken from the Gemini Multi Object Spectrometers (Worseck et al. 2014), and at $z = 2$–4 with both space- and ground-based facilities (Prochaska et al. 2009; Fumagalli et al. 2013; O'Meara et al. 2013). These studies find that the mean free path increases with decreasing redshift, from $\sim 10\ h_{70}^{-1}$ Mpc at $z \simeq 5$ to more than 200 h_{70}^{-1} Mpc at $z \simeq 2.4$. Yet, only two direct $\lambda_{\rm mfp}^{912}$ estimates are available in the redshift range $z = 2$–3 (i.e., Fumagalli et al. 2013; O'Meara et al. 2013) because, at $z < 2.5$, one must consider space-based spectroscopy to cover the rest-frame wavelength blueward of 912 Å.

The structure of this paper is as follows. We discuss the sample, the selection criteria, and the data reduction of the quasar pairs in our *HST* survey in Section 2. In Section 3 we describe the technique to construct the stacked spectrum, and the IGM transmission curves adopted to correct the observed average spectrum are presented in Section 4, where we also describe our IGM-corrected stack along with its uncertainties. The formalism considered in the estimate of the mean free path to ionizing photons is presented in Section 5. Section 6 describes how we model absorbers in our sample, and the discussion on the implications of our analysis and conclusions is presented in Section 7.

We adopt a concordance flat Λ cosmology with $H_0 = 70\ {\rm km\ s^{-1}\ Mpc^{-1}}$, $\Omega_{\rm m} = 0.3$, and $\Omega_\Lambda = 0.7$. Unless noted otherwise, we will distinguish between the ionizing and nonionizing parts of the spectrum as $\lambda < 912$ Å and 912–2000 Å, respectively.

2. The Data Set

The sample of quasars observed in our *HST* program is drawn from a compilation of quasar pairs with $g^* < 21$ mag (Hennawi et al. 2006a, 2010; Findlay et al. 2018), selected from the SDSS/BOSS footprints in the redshift range $z \simeq 2.0$–2.5. Six quasar lenses with comparable magnitudes and redshifts are also observed during our campaign but excluded for this analysis. Our *HST* program includes 47 quasar pairs and four additional single quasars observed within the survey, leading to a total of 104 quasars (111 observations[11]). Roughly 50% of the quasars within the survey have spectroscopic redshifts from SDSS, while the rest have redshift measurements from our follow-up optical campaign. Table 1 lists the 111 observations for the whole WFC3 sample of 104

[11] We obtained 94 spectra for the quasar pairs, 13 spectra for the lenses, and four additional spectra for the single quasars, for a total of 111 observations.

Table 1
Full Sample of WFC3 Quasars

Name	R.A. (J2000) (degrees)	Decl. (J2000) (degrees)	u^*	g^*	r^*	i^*	z^*	$R_\perp$ (kpc)	$\Delta\theta$ ($''$)	z	σ_z (km s^{-1})	em. line[a]	Instr.[b]	Note
SDSS J002423.88–012827.6	6.099520	−1.474347	19.11	18.91	18.76	18.67	18.51	46.2	5.34	2.047	275	Mg II	MagE	…
SDSS J002424.21–012825.7	6.100912	−1.473832	19.03	18.93	18.84	18.72	18.52	46.2	5.34	2.058	657	C IV–C III]	MagE	…
SDSS J011707.51+315341.1	19.281323	31.894773	20.83	20.03	19.81	19.79	19.49	94.1	11.32	2.639	28	…	BOSS	…
SDSS J011708.38+315338.6	19.284939	31.894074	21.66	20.78	20.60	20.68	20.39	94.1	11.32	2.624	40	…	BOSS	…
SDSS J013458.85+243050.5	23.745247	24.514045	21.03	20.43	20.18	20.09	19.77	31.8	3.69	2.105	56	…	BOSS	…
SDSS J013459.01+243047.5	23.745903	24.513213	20.28	19.85	19.60	19.53	19.28	31.8	3.69	2.095	53	…	BOSS	…
HE0230–2130	38.138119	−21.290540	…	…	…	…	…	…	…	2.163	284	…	ref	lens[c]
HE0230–2130	38.138473	−21.290031	…	…	…	…	…	…	…	2.163	284	…	ref	lens[c]
HE0230–2130	38.138325	−21.290467	…	…	…	…	…	…	…	2.163	284	…	ref	lens
SDSS J034406.64+101509.8	56.027689	10.252729	20.85	20.52	20.12	19.84	19.51	105.2	12.11	2.018	656	C IV–C III]	KPNO	…
SDSS J034407.03+101520.5	56.029300	10.255699	19.94	19.54	19.20	18.98	18.72	105.2	12.11	2.002	519	Si IV–C IV–C III]	KPNO	…
SDSS J073522.43+295710.2	113.843476	29.952837	21.05	20.53	20.38	20.24	20.21	47.0	5.44	2.082	798	C IV	ESI	…
SDSS J073522.55+295705.0	113.843980	29.951404	20.77	20.37	20.07	19.87	19.56	47.0	5.44	2.065	274	Mg II	ESI	…
SDSS J074653.04+440351.4	116.720790	44.064326	18.87	18.81	18.75	18.45	18.15	8.7	1.08	2.008	27	…	SDSS	lens[c]
SDSS J074653.04+440351.4	116.721160	44.064181	18.87	18.81	18.75	18.45	18.15	8.7	1.08	2.008	27	…	SDSS	lens
SDSS J081329.49+101405.2	123.372873	10.234790	19.67	19.41	19.34	19.14	18.90	61.7	7.13	2.098	629	Si IV–C IV	MagE	…
SDSS J081329.70+101411.6	123.373778	10.236561	20.13	20.09	20.03	19.85	19.75	61.7	7.13	2.071	273	Mg II	MagE	…
SDSS J084624.33+270958.3	131.601376	27.166211	21.08	20.82	20.67	20.54	20.26	39.9	4.65	2.203	655	C IV–C III]	ESI	…
SDSS J084624.50+271002.4	131.602116	27.167341	20.94	20.37	20.48	20.47	20.18	39.9	4.65	2.195	27	…	BOSS	…
SDSS J085230.22+350003.6	133.125924	35.001018	20.71	20.36	20.36	20.36	20.02	45.1	5.27	2.238	518	Si IV–C IV–C III]	ESI	…
SDSS J085230.53+350000.0	133.127220	35.000008	20.49	19.97	19.93	19.90	19.52	45.1	5.27	2.235	22	…	BOSS	…
SDSS J092056.00+131102.6	140.233359	13.184074	20.00	19.22	19.23	19.19	18.94	52.5	6.21	2.427	796	C IV	MagE	…
SDSS J092056.23+131057.4	140.234319	13.182618	19.89	19.31	19.49	19.42	19.09	52.5	6.21	2.446	792	C IV	MagE	…
SDSS J093747.24+150928.0	144.446866	15.157782	20.78	20.04	19.98	19.95	19.59	98.3	11.75	2.555	523	Si IV–C IV–C III]	MagE	…
SDSS J093747.40+150939.5	144.447531	15.160981	20.42	19.92	19.80	19.83	19.59	98.3	11.75	2.541	35	…	BOSS	…
SDSS J100233.90+353127.5	150.641268	35.524327	19.37	18.86	18.82	18.84	18.62	33.3	3.91	2.305	39	…	BOSS	…
SDSS J100234.21+353128.6	150.642548	35.524634	20.84	20.05	20.02	19.90	19.76	33.3	3.91	2.320	795	C IV	ESI	…
SDSS J101652.88+222412.1	154.220347	22.403368	20.24	20.29	20.35	20.08	19.77	128.5	14.81	2.031	791	C IV	CAHA	…
SDSS J101653.94+222413.7	154.224775	22.403806	21.01	20.94	20.64	20.31	20.00	128.5	14.81	2.017	994	C IV	WCF3	…
Q1017–207	154.349680	−20.783085	…	…	…	…	…	…	…	2.545	254	…	ref	lens[c]
Q1017–207	154.349930	−20.783091	…	…	…	…	…	…	…	2.545	254	…	ref	lens
SDSS J103424.76+330624.1	158.603203	33.106711	20.97	20.73	20.67	20.57	20.10	101.5	11.71	2.010	996	C IV	WFC3	…
SDSS J103425.08+330635.1	158.604527	33.109769	19.44	19.35	19.33	19.32	19.17	101.5	11.71	2.023	79	…	SDSS	…
SDSS J104533.31+404137.9	161.388830	40.693886	20.90	20.41	20.43	20.32	20.13	145.8	17.05	2.261	27	…	BOSS	…
SDSS J104533.54+404121.1	161.389760	40.689207	21.03	20.26	20.24	20.16	19.92	145.8	17.05	2.286	40	…	BOSS	…
SDSS J105644.88–005933.4	164.187008	−0.992616	20.48	20.09	20.02	19.90	19.66	62.2	7.21	2.135	660	C III]	MagE	…
SDSS J105645.24–005938.1	164.188530	−0.993918	21.18	20.96	20.83	20.78	20.58	62.2	7.21	2.126	518	Si IV–C IV–C III]	MagE	…
SDSS J110430.00+290753.4	166.125030	29.131523	20.74	20.35	20.26	20.18	19.92	54.5	6.32	2.133	38	…	BOSS	…
SDSS J110430.34+290749.0	166.126455	29.130283	21.14	20.49	20.29	20.25	20.16	54.5	6.32	2.127	0	…	BOSS	…
SDSS J111641.79+650717.2	169.174126	65.121465	21.71	21.06	21.01	22.00	20.44	51.4	6.04	2.311	53	…	BOSS	…
SDSS J111642.55+650720.9	169.177312	65.122475	21.27	20.54	20.62	20.28	19.90	51.4	6.04	2.308	652	C IV–C III]	LRIS	…
SDSS J112455.24+571056.5	171.230202	57.182383	19.35	18.56	18.74	18.62	18.35	18.8	2.21	2.311	26	…	BOSS	…
SDSS J112455.44+571058.1	171.230999	57.182811	20.54	19.92	19.83	19.71	19.33	18.8	2.21	2.320	722	Si IV–C IV	MMT	…
SDSS J113947.06+414351.1	174.946097	41.730875	20.89	20.22	20.03	19.78	19.37	20.4	2.39	2.202	58	…	BOSS	…
SDSS J113947.25+414352.1	174.946912	41.731139	20.67	19.98	19.80	19.44	19.03	20.4	2.39	2.239	648	C IV	ESI	…
SDSS J114504.35+285713.0	176.268160	28.953626	21.14	20.68	20.73	20.63	20.68	35.1	4.09	2.174	42	…	BOSS	…
SDSS J114504.66+285712.6	176.269454	28.953521	20.78	20.35	20.10	20.01	19.87	35.1	4.09	2.167	795	C IV	KPNO	…

Table 1
(Continued)

Name	R.A. (J2000) (degrees)	Decl. (J2000) (degrees)	u^*	g^*	r^*	i^*	z^*	$R_\perp$ (kpc)	$\Delta\theta$ ($''$)	z	σ_z (km s^{-1})	em. line[a]	Instr.[b]	Note
SDSS J115031.14+045353.2	177.629760	4.898127	21.48	20.58	20.37	20.37	20.14	58.4	6.96	2.527	518	Si IV–C IV–C III]	MagE	⋯
SDSS J115031.54+045356.8	177.631427	4.899124	21.20	20.52	20.38	20.39	20.18	58.4	6.96	2.517	28	⋯	BOSS	⋯
SDSS J121645.92+352941.5	184.191355	35.494881	20.50	20.40	20.26	19.96	19.78	⋯	⋯	2.017	52	⋯	SDSS	lens[c]
SDSS J121646.04+352941.5	184.191862	35.494861	19.52	19.38	19.19	19.06	18.85	⋯	⋯	2.017	52	⋯	SDSS	lens
SDSS J122545.23+564445.0	186.438466	56.745842	21.33	20.70	20.62	20.50	19.98	51.2	6.05	2.393	40	⋯	BOSS	⋯
SDSS J122545.73+564440.5	186.440546	56.744607	20.13	19.37	19.47	19.42	19.16	51.2	6.05	2.386	1	⋯	BOSS	⋯
SDSS J123635.14+522058.8	189.146430	52.349670	21.20	20.63	20.42	20.47	20.35	25.7	3.07	2.567	521	Si IV–C IV–C III]	ESI	⋯
SDSS J123635.42+522057.0	189.147585	52.349185	21.59	20.49	20.51	20.75	20.18	25.7	3.07	2.578	14	⋯	BOSS	⋯
SDSS J125420.52+610435.7	193.585516	61.076602	19.67	19.57	19.41	19.26	19.09	151.4	17.60	2.036	39	⋯	BOSS	⋯
SDSS J125421.98+610421.7	193.591607	61.072701	19.25	19.07	18.99	18.90	18.71	151.4	17.60	2.051	70	⋯	SDSS	⋯
SDSS J133145.98+033546.2	202.941610	3.596176	20.85	20.31	20.29	20.30	20.26	27.6	3.30	2.579	37	⋯	BOSS	⋯
SDSS J133146.19+033545.4	202.942482	3.595964	21.84	21.12	21.14	21.05	21.39	27.6	3.30	2.584	836	Lyα	MMT	⋯
SDSS J133209.26+252301.3	203.038616	25.383711	20.31	20.13	20.02	19.90	19.65	68.4	7.92	2.080	652	C IV–C III]	ESI	⋯
SDSS J133209.69+252306.8	203.040375	25.385231	20.07	20.09	20.12	19.97	19.62	68.4	7.92	2.093	649	C IV–C III]	ESI	⋯
SDSS J133221.71+471721.3	203.090460	47.289273	21.52	20.76	20.87	20.98	20.61	80.9	9.50	2.312	34	⋯	BOSS	⋯
SDSS J133222.03+471712.4	203.091828	47.286801	21.19	20.65	20.53	20.46	20.32	80.9	9.50	2.310	58	⋯	BOSS	⋯
SDSS J133831.53+001056.2	204.631394	0.182282	21.35	20.59	20.73	20.68	20.46	99.3	11.64	2.300	908	C IV	WFC3	⋯
SDSS J133831.96+001105.9	204.633186	0.184976	21.23	20.92	20.96	20.90	20.78	99.3	11.64	2.297	33	⋯	BOSS	⋯
SDSS J133904.10+374742.3	204.767099	37.795098	21.34	20.90	20.80	20.81	20.66	54.2	6.32	2.187	941	⋯	CAHA	⋯
SDSS J133904.46+374737.7	204.768612	37.793813	21.66	21.02	20.92	20.84	20.53	54.2	6.32	2.196	61	⋯	BOSS	⋯
SDSS J133905.25+374755.3	204.771883	37.798711	21.55	21.60	21.68	21.25	21.96	⋯	⋯	1.810	1067	C IV	WFC3	[d]
SDSS J133907.13+131039.6	204.779743	13.177685	19.14	18.64	18.77	18.67	18.76	14.5	1.70	2.239	28	⋯	SDSS	⋯
SDSS J133907.23+131038.7	204.780142	13.177416	19.58	19.16	19.00	18.95	18.51	14.5	1.70	2.237	21	⋯	BOSS	⋯
SDSS J134543.64+262506.9	206.431832	26.418598	20.28	20.27	20.26	19.96	19.70	79.9	9.22	2.038	276	Mg II	ESI	⋯
SDSS J134544.31+262505.3	206.434650	26.418155	19.96	19.97	19.51	19.16	18.94	79.9	9.22	2.016	517	Si IV–C IV–C III]	ESI	BAL
SDSS J140052.07+123235.2	210.216976	12.543120	20.54	20.36	20.31	20.17	19.95	126.4	14.60	2.058	794	C IV	WFC3	⋯
SDSS J140052.55+123248.0	210.218986	12.546672	20.66	20.49	20.47	20.29	19.97	126.4	14.60	2.071	791	C IV	WFC3	⋯
SDSS J140953.74+392000.1	212.473921	39.333362	20.28	20.17	20.15	20.07	19.97	59.0	6.82	2.058	794	C IV	WFC3	⋯
SDSS J140953.87+391953.4	212.474488	39.331517	21.05	20.78	20.82	20.49	20.39	59.0	6.82	2.088	796	C IV	WFC3	⋯
SDSS J142148.79+163017.5	215.453308	16.504886	21.02	20.40	20.35	20.38	20.26	84.4	10.02	2.457	113	⋯	BOSS	⋯
SDSS J142149.00+163027.1	215.454200	16.507535	21.62	20.76	20.56	20.62	20.42	84.4	10.02	2.463	29	⋯	BOSS	⋯
SDSS J143104.64+270524.6	217.769363	27.090177	20.57	19.80	19.90	19.76	19.57	50.7	5.94	2.266	14	⋯	BOSS	⋯
SDSS J143104.97+270528.6	217.770735	27.091286	20.91	20.26	20.28	20.17	19.97	50.7	5.94	2.263	524	Si IV–C IV–C III]	ESI	⋯
SDSS J144254.60+405535.0	220.727519	40.926407	20.38	19.12	18.68	18.34	17.99	⋯	⋯	2.575	11	⋯	BOSS	lens[c]
SDSS J144254.78+405535.5	220.728257	40.926553	19.60	18.51	18.12	17.92	17.61	⋯	⋯	2.575	11	⋯	BOSS	lens
SDSS J144320.92+200825.4	220.837190	20.140400	20.12	19.32	19.14	19.03	18.98	97.3	11.73	2.654	18	⋯	BOSS	⋯
SDSS J144321.03+200813.8	220.837665	20.137169	21.66	20.80	20.64	20.79	20.37	97.3	11.73	2.672	20	⋯	BOSS	⋯
SDSS J151538.47+151134.8	228.910324	15.193007	19.01	18.58	18.56	18.35	18.21	⋯	⋯	2.051	11	⋯	BOSS	lens[c]
SDSS J151538.59+151135.9	228.910805	15.193315	18.28	18.26	18.22	18.03	17.79	⋯	⋯	2.051	11	⋯	BOSS	lens
SDSS J154815.42+284452.6	237.064263	28.747970	21.07	20.49	20.62	20.79	20.82	⋯	⋯	2.305	38	⋯	BOSS	[d]
SDSS J154938.17+313646.8	237.409048	31.613024	21.10	20.12	20.18	20.12	19.83	108.6	12.96	2.520	15	⋯	BOSS	⋯
SDSS J154938.49+313634.6	237.410398	31.609612	20.12	19.29	19.09	19.09	18.92	108.6	12.96	2.502	651	C IV–C III]	ESI	⋯
SDSS J161301.69+080806.0	243.257052	8.135014	20.17	19.56	19.53	19.47	19.29	81.6	9.64	2.382	20	⋯	BOSS	⋯
SDSS J161302.03+080814.2	243.258469	8.137295	19.51	18.91	18.84	18.80	18.61	81.6	9.64	2.387	17	⋯	BOSS	⋯
SDSS J163700.87+263613.7	249.253855	26.602753	20.99	20.70	20.68	20.43	20.23	33.5	3.85	1.961	273	⋯	ESI	⋯
SDSS J163700.92+263609.9	249.253654	26.603810	19.67	19.40	19.26	19.17	19.07	33.5	3.85	1.965	84	⋯	SDSS	⋯
SDSS J171945.87+254951.2	259.941135	25.830905	20.26	19.87	19.75	19.73	19.56	126.2	14.68	2.175	944	⋯	WFC3	⋯

Table 1
(Continued)

Name	R.A. (J2000) (degrees)	Decl. (J2000) (degrees)	u^*	g^*	r^*	i^*	z^*	$R_\perp$ (kpc)	$\Delta\theta$ ($''$)	z	σ_z (km s^{-1})	em. line[a]	Instr.[b]	Note
SDSS J171946.66+254941.1	259.944429	25.828104	20.34	20.05	19.99	19.92	19.68	126.2	14.68	2.172	39	⋯	BOSS	⋯
SDSS J172855.24+263449.1	262.230176	26.580311	20.11	19.82	19.59	19.35	19.24	77.5	9.07	1.806	1068	⋯	WFC3	[d]
SDSS J172855.31+263458.1	262.230485	26.582816	20.65	20.14	20.01	19.94	19.76	77.5	9.07	2.260	31	⋯	SDSS	[d]
SDSS J210329.25+064653.3	315.871874	6.781478	21.47	20.60	20.44	20.53	20.26	31.8	3.80	2.574	629	Si IV–C III]	MagE	⋯
SDSS J210329.37+064649.9	315.872385	6.780550	21.23	20.22	20.07	20.00	19.66	31.8	3.80	2.565	790	Si IV	MagE	⋯
SDSS J221426.79+132652.3	333.611628	13.447874	20.87	20.58	20.36	20.07	19.78	50.7	5.84	2.000	270	Mg II	GMOS	⋯
SDSS J221427.03+132657.0	333.612634	13.449171	20.57	20.34	20.25	20.00	19.55	50.7	5.84	1.998	270	Mg II	GMOS	⋯
SDSS J224136.99+230909.8	340.404141	23.152724	20.58	19.87	19.88	19.79	19.59	74.7	8.81	2.371	53	⋯	BOSS	⋯
SDSS J224137.03+230901.0	340.404323	23.150281	21.48	20.77	20.59	20.64	20.14	74.7	8.81	2.374	889	⋯	WFC3	⋯
SDSS J224204.37+055828.6	340.518218	5.974627	21.58	21.05	20.68	20.47	20.09	35.7	4.27	2.525	791	C IV	GMOS	⋯
SDSS J224204.63+055830.4	340.519297	5.975129	21.41	20.61	20.40	20.37	20.34	35.7	4.27	2.511	28	⋯	BOSS	⋯
SDSS J224325.04–061350.3	340.854357	−6.230640	21.29	20.83	20.77	20.69	20.45	78.9	9.46	2.602	791	C IV	GMOS	⋯
SDSS J224325.67–061350.9	340.856994	−6.230824	19.80	19.13	19.09	19.00	18.68	78.9	9.46	2.597	525	Si IV–C IV–C III]	MagE	⋯
SDSS J224856.83+030700.2	342.236798	3.116728	21.66	20.87	20.75	20.73	20.66	50.5	5.96	2.394	43	⋯	BOSS	⋯
SDSS J224857.22+030659.5	342.238446	3.116531	21.40	20.61	20.49	20.46	20.30	50.5	5.96	2.395	147	⋯	BOSS	⋯
SDSS J234819.19+005717.5	357.079959	0.954877	20.98	20.63	20.54	20.45	20.28	60.9	7.07	2.153	52	⋯	BOSS	⋯
SDSS J234819.58+005721.4	357.081604	0.955965	19.19	18.84	18.75	18.71	18.50	60.9	7.07	2.159	44	⋯	SDSS	⋯

Notes: All magnitudes quoted here are SDSS magnitudes (no Galactic extinction applied). The column labeled $R_\perp$ is the transverse proper separation in kpc, while $\Delta\theta$ is the angular separation in arcseconds. Redshifts along with their uncertainties (in km s^{-1}) are listed in the columns labeled z and σ_z, respectively.

[a] Emission lines considered for the redshift estimates.

[b] Survey/instrument/telescope considered for the quasar redshift. The relative reference is provided in the case a source already has a redshift available from the literature. * = Anguita et al. (2008), ** = Claeskens et al. (1996), Surdej et al. (1997).

[c] Lower S/N lens spectrum that has been excluded from the stacking analysis.

[d] SDSS J133905.25+374755.3 and SDSS J154815.42+284452.6 are single field quasars observed during our survey. The system SDSS J172855.24+263449.1 and SDSS J172855.31+263458.1 is a projected pair with line-of-sight velocity separations >11,000 km s^{-1}, thus not included in quasar pair analysis.

(This table is available in machine-readable form.)

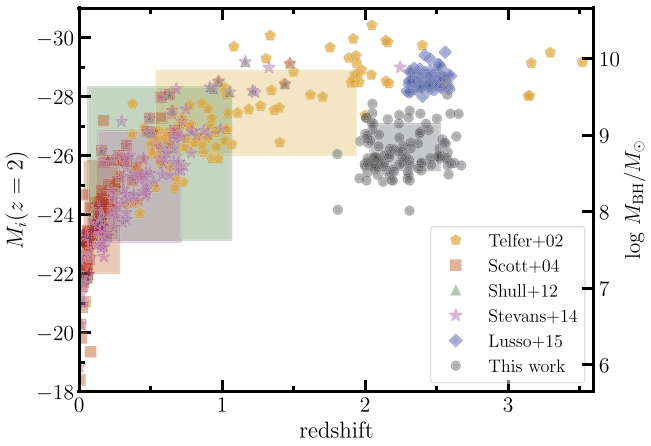

Figure 1. Absolute i-band magnitude (normalized at $z = 2$, K-corrected following Richards et al. 2006) as a function of redshift. Symbols represent different literature samples: T02 (orange pentagons), S04 (red squares), S12 (green triangles), S14 (magenta stars), L15 WFC3 sample (blue diamonds), and our new WFC3 quasar pair sample (black circles). Shaded areas indicate the redshift and magnitude ranges for the different samples, estimated from the 16th and 84th percentiles. Approximate values of the black hole masses (in units of $M_\odot$) are plotted on the y axis on the right.

quasars. In the present analysis, we will focus on the properties of the 47 quasar pairs only. We will present further results on the properties of the intervening absorbers, including their autocorrelation function, from the entire survey in a forthcoming publication.

To compare our new WFC3 quasar pair sample with previous works in the literature, we computed the absolute i-band magnitude, $M_i(z = 2)$, from the observed SDSS i^*, normalized at $z = 2$, and K-corrected following Richards et al. (2006). Figure 1 shows the distribution of $M_i(z = 2)$ as a function of redshift for several single quasar samples from the literature, from which the composite AGN spectra were constructed. We also plotted indicative values of the black hole masses (in units of $M_\odot$) on the y axis on the right, where M_{BH} is estimated via $\lambda_{Edd} = L_{bol}/L_{Edd}$ assuming an average $\lambda_{Edd} = 0.35$. The relation between L_{bol} and $M_i(z = 2)$ has been estimated to be $\log L_{bol} = -10.03\ M_i(z = 2)/26 + 36.33$ by fitting the quasars in the SDSS-DR7 quasar catalog (Shen et al. 2011). The samples included in this comparison are the Lusso et al. (2015; L15 hereafter) WFC3 sample (blue diamonds), Stevans et al. (2014, S14 hereafter; magenta stars), Shull et al. (2012, S12 hereafter; green triangles), Telfer et al. (2002; orange pentagons), and Scott et al. (2004, S04 hereafter; red squares). Shaded areas indicate the redshift and magnitude ranges for the different samples, estimated from the 16th and 84th percentiles. Our new WFC3 quasar pair data set is at a similar redshift range ($1.961 \leqslant z \leqslant 2.673$) as that considered by L15 ($z \simeq 2.440$; O'Meara et al. 2011, 2013), with a mean (median) redshift of $\langle z \rangle \simeq 2.256(2.237)$, while probing lower luminosity quasars.

2.1. Data Reduction

Each quasar pair was observed with *HST* WFC3/UVIS for one orbit between 2016 September and 2017 March 12 (Cycle 23, program ID 14127, PI: Fumagalli). Every visit consisted of one F300X direct image of 100 s and two G280 dispersed images of 1200 s each, to enable cleaning the images of cosmic rays. The only exceptions are J224136+230909 and J210329+064653, which have just one direct image of 240 s each. To correct for the charge transfer efficiency (CTE) degradation of the detector, the raw images were processed with WFC3UV_CTEREVERSE[12] for a pixel-based CTE correction based on modeling of hot pixels (Anderson & Bedin 2010; Massey et al. 2010).

We created custom dark reference files to correct for dark current structure and to mitigate hot pixels. Specifically, for optimal dark subtraction and hot pixel identification, we created superdark files as detailed in Rafelski et al. (2015) and Vasei et al. (2016). These superdark files are similar to those currently produced at the Space Telescope Science Institute (STScI, WFC3 ISR 2016–08), but they also include the use of concurrent darks as the observations and improved hot pixel rejection, which is important for our program due to the small number of exposures obtained. In particular, our methodology models the dark background with a third-order polynomial to remove the background gradient temporarily before identifying hot pixels, enabling the detection of a uniform number of hot pixels both far from and close to the readout of each chip. The resultant science files are CTE corrected with reduced background gradients, blotchy patterns, and appropriate hot pixel flagging (Rafelski et al. 2015).

Cosmic-ray rejection was performed by building an association table for each pair of exposures and using the CALWF3 built-in cosmic-ray rejection called WF3REJ. No cosmic-ray rejection was done for the direct images of J224136+230909 and J210329+064653, and centers of the pairs for these two targets were identified manually to avoid issues related to cosmic rays. The resultant calibrated and cosmic-ray-cleaned images are utilized in the extraction described below.

2.2. Wavelength and Flux Calibration

To extract 1D spectra from the G280 dispersed images, we used an updated version of the pipeline discussed in O'Meara et al. (2011). The pipeline makes use of the latest calibration files provided by the aXe team.[13] Major changes to the pipeline include the use of both ±1 orders (which we will refer to as beam A and beam C in accordance with the nomenclature used in the literature), improved wavelength and trace solutions away from the chip center, and an improved extraction algorithm. The pipeline is provided as part of the publicly available XIDL software package.[14]

In detail, the pipeline first considers the direct image to find the center of the emission around a user-supplied R.A. and decl. using the IDL routine *cntrd*. The position of the center of emission is then employed to calculate an initial trace and wavelength solution for the individual beams using the updated calibrations supplied by the aXe team. These solutions are sixth- and fourth-order polynomial functions that vary smoothly as a function of position on the chip.

After finding these initial trace solutions, the pipeline calculates the offset between this trace and the Gaussian centroid of the data for each individual column. The median offset for each individual beam is calculated, and the trace is offset by this amount. For beam C, below a wavelength of ∼3000 Å, we found significant deviations between the centroid of the data and the adjusted trace. For these data columns, we

[12] http://www.stsci.edu/hst/wfc3/tools/cte_tools
[13] http://www.stsci.edu/hst/wfc3/analysis/grism_obs/calibrations/wfc3_g280.html
[14] https://github.com/profxj/xidl.git

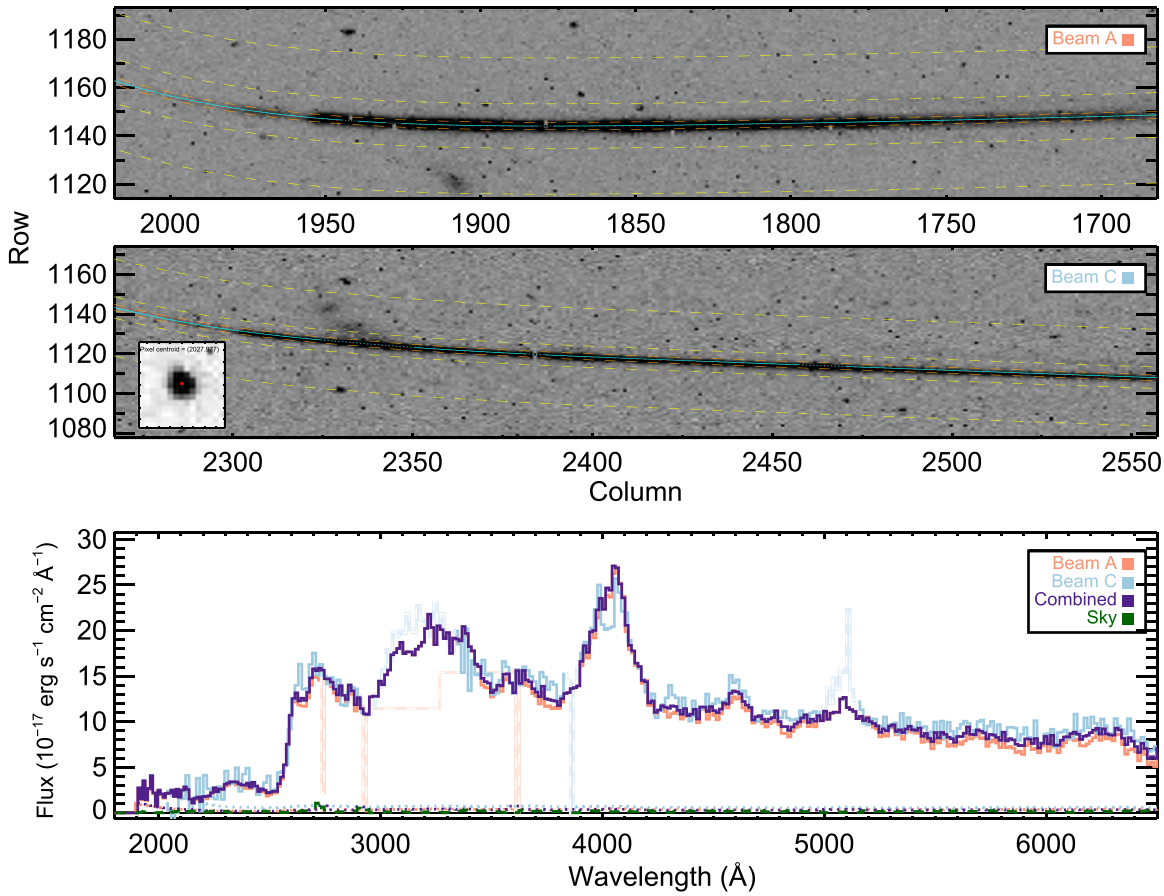

Figure 2. WFC3/G280 grism exposure and flux-calibrated spectra of the quasar SDSS J100233.9+353127.5. Upper two panels: the first-order dispersed spectrum on the top panel (beam A) and the −1st-order spectrum on the bottom (beam C). The zeroth-order image of the quasar is shown on the bottom left side of the beam C panel. The bottom panel shows the fluxed 1D spectra for beam A (red), beam C (cyan), and for the combined beams (purple).

(The complete figure set (111 images) is available.)

fit the residual offsets with a third-order polynomial and apply this offset. We note that this step produces errors in the wavelength calibration on the order of ∼10%, and when coadding the beams, we use beam C mainly as a substitute when the primary beam A is affected by chance superposition with other sources or detector artifacts.

Sky subtraction is performed on a 20-pixel-wide region of blank sky above and below the trace of each of the individual beams. For close quasar pairs or lensed quasars, only a single sky region (the region not containing the spectrum of the other sight line) is used. All features above 2.5σ in the sky region are clipped, and the 1D sky spectrum is smoothed by a zeroth-order SAVGOL filter. This sky model is then subtracted from all pixels in the corresponding beam.

A variance image is created, assuming Gaussian statistics and a read noise of 3.3 electrons per exposure. The final 1D spectrum for each of the beams is extracted from this sky-subtracted image using optimal extraction, which assumes a Gaussian profile for the spectrum. The resultant 1D spectrum for each of the individual beams is then fluxed using the calibration files supplied by the aXe team.

Next, the two fluxed 1D spectra of the individual beams are visually inspected, and regions of the spectra containing bad pixels or interloping zeroth-order emission from unrelated galaxies are masked. Finally, the two beams are combined using the XIDL routine *long_combspec*. This routine interpolates the data onto a common wavelength grid, clips any outliers, and performs an average of the two beams, weighting by the S/N. Figure 2 presents the 2D spectral image (sky subtracted) and the fluxed 1D spectrum for beam A and beam C for one source. The fluxed 1D spectrum for the combined beams is also shown.

To further check our flux calibration, we have estimated the observed g^*-band magnitude from the WFC3 spectra and compared this value with the one obtained from either the SDSS or the BOSS survey for all quasars with an optical spectrum[15] (53 quasars). The difference between these magnitudes ($\Delta g^* = g^*_{\rm WFC3} - g^*$) does not display strong systematics, with a mean (median) Δg^* of about 0.05 (0.03) and a dispersion around the mean of 0.16 dex. SDSS/BOSS observations were carried out between 2002 and 2013, so part of this scatter may be due to intrinsic long-term UV variability (MacLeod et al. 2012).

2.3. Redshift Estimates

Optical spectra were obtained for a fraction of our quasar pairs from a variety of instruments and thus have different wavelength coverage and resolution. High S/N spectra were taken for 27 quasars using the Echellette Spectrograph and

[15] For quasars with multiple spectra, we have selected the one with the highest S/N per resolution element.

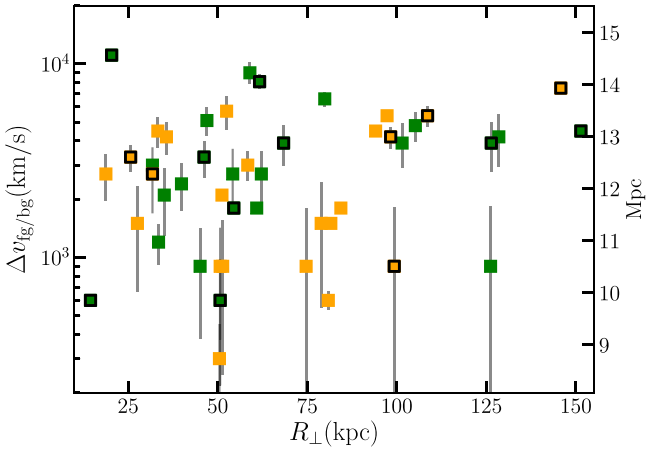

Figure 3. Range of relative velocities between the foreground and background quasar pair ($\Delta v_{\rm fg/bg} = c|z_{\rm fg}-z_{\rm bg}|$) and their proper transverse separations. The physical distances in Mpc are plotted on the y axis on the right. The green and orange squares represent the low-redshift ($\langle z\rangle = 2.09$) and high-redshift ($\langle z\rangle = 2.44$) quasar subsamples, respectively. The quasars with at least one absorber ($\log N_{\rm H\,I} > 17.2$) within 5000 km s^{-1} are marked with open black squares (see discussion in Sections 6 and 7.1).

Imager (ESI) at the Keck II telescope and the moderate-resolution Magellan Echellette (MagE) optical spectrograph. Twelve quasars have medium- to low-resolution optical spectroscopy from several telescopes, such as the 6.5 m Multiple Mirror Telescope (MMT), Calar Alto Observatory (CAHA), Keck, the 2.1 m telescope at the Kitt Peak National Observatory (KPNO), and Gemini (see Table 1). All of the observed quasars have both the Lyα and C IV lines covered. The ESI spectra are always considered for redshift determination when available, otherwise we use BOSS/SDSS redshifts (50% of the sample) or the low-S/N spectra. Details on the observations and data reduction will be provided in a separate paper, as here we only use these spectra for redshift determination of the quasars and the absorbers. At the time of writing, 11 quasars do not have any spectra other than those taken with *HST* WFC3/UVIS. The redshifts of these objects were determined from the C IV line observed by WFC3, so these have the least precise measurements ($\sigma_z \simeq 800$–1000 km s^{-1}). For the two lensed quasars HE0230–2130 and Q1017–207, the redshift was taken from the literature (Claeskens et al. 1996; Surdej et al. 1997; Anguita et al. 2008).

To compute the redshift, we have followed a procedure similar to the one described by Hennawi et al. (2006a). Lines were fitted as the sum of a Gaussian plus a linear local continuum using a custom-made IDL code. Strong absorption or noisy features were masked. For the majority of the sources, the redshift was estimated from the C IV line only,[16] but there were cases (19 quasars) in which that line was used in combination with other emission lines, like the Si IV and the semiforbidden C III] lines. For six quasars in which the Mg II broad emission line was also covered, we have computed the redshift from that line only, as this is considered a better tracer of the systemic redshift (Richards et al. 2002).

[16] We note that redshifts estimated using high-ionization broad emission lines, such as C IV and Lyα, could be shifted blueward with respect to the systemic (e.g., >500–1000 km s^{-1}; Gaskell 1982; Espey et al. 1989; Corbin 1990).

The distribution of radial velocity differences between the foreground and background quasars in the pair ($\Delta v_{\rm fg/bg} = c|z_{\rm fg} - z_{\rm bg}|$) as a function of their proper transverse separations is shown in Figure 3. Given the sample selection (i.e., we observed the closest projected pairs with similar spectroscopic redshift), the bulk of the quasar pair sample is clustered at small velocity differences ($\Delta v_{\rm fg/bg} < 4000$ km s^{-1}), which translates into physical distances of <15 Mpc. The redshifts and the emission lines considered for their estimates are listed in Table 1 along with the associated (statistical) uncertainties.

3. Composite Quasar Spectrum

The spectral stack for the WFC3 quasar pairs is constructed following an approach similar to the one in L15. In the WFC3 data, the observed wavelengths shorter than ∼2100 Å and longer than 6500 Å are trimmed because the sensitivity of the G280 detector declines rapidly at those wavelengths, leading to complicated systematic effects and artifacts. To construct the quasar spectral stack, we use the observed spectrum obtained by combining the two beams as the reference. The procedure we follow is outlined below:

1. We correct the quasar flux density[17] (f_λ) for Galactic reddening by adopting the $E(B-V)$ estimates from Schlafly & Finkbeiner (2011), whose median reddening value is $E(B-V) \simeq 0.03$ mag, and the Galactic extinction curve from Fitzpatrick (1999) with $R_V = 3.1$. We do not correct the spectra for intrinsic dust absorption, as this is a relatively high-redshift ($z > 2$), optically selected quasar sample, and thus intrinsic reddening is expected to be small.
2. We generate a rest-frame wavelength array with fixed dispersion $\Delta\lambda$. The dispersion value was set to be large enough to include at least one entire pixel from the WFC3/UVIS-G280 spectra at rest wavelengths $\lambda < 1215$ Å (i.e., $\Delta\lambda \simeq 6.2$Å).
3. Each quasar spectrum was shifted to the rest frame and rebinned over the common rest-frame wavelength array.[18] Given our adopted masking ($2100 < \lambda_{\rm obs} < 6500$ Å), the final rest-frame wavelength range where almost all objects are contributing in each flux bin is restricted to 700–2000 Å.
4. We normalized individual spectra by their flux at rest wavelength $\lambda = 1450$ Å.
5. All of the flux values at each wavelength were then averaged (mean) to produce the stacked spectrum normalized to unity at $\lambda = 1450$ Å.

Uncertainties on the observed stack are estimated through a bootstrap resampling technique. We created 10,000 random samples of the quasar spectra with replacement, and we applied the same procedure as described above.

3.1. Comparison to the L15 WFC3 Composite for Single Quasars

The quasar sample employed by L15 was drawn from a similar survey performed with *HST* using the low-resolution

[17] In the following, we will use the word "flux" to mean the flux density (i.e., flux per unit wavelength).

[18] Wavelengths are divided by $(1+z)$ to shift the spectra into the source rest frame, while fluxes in f_λ are multiplied by $(1+z)$.

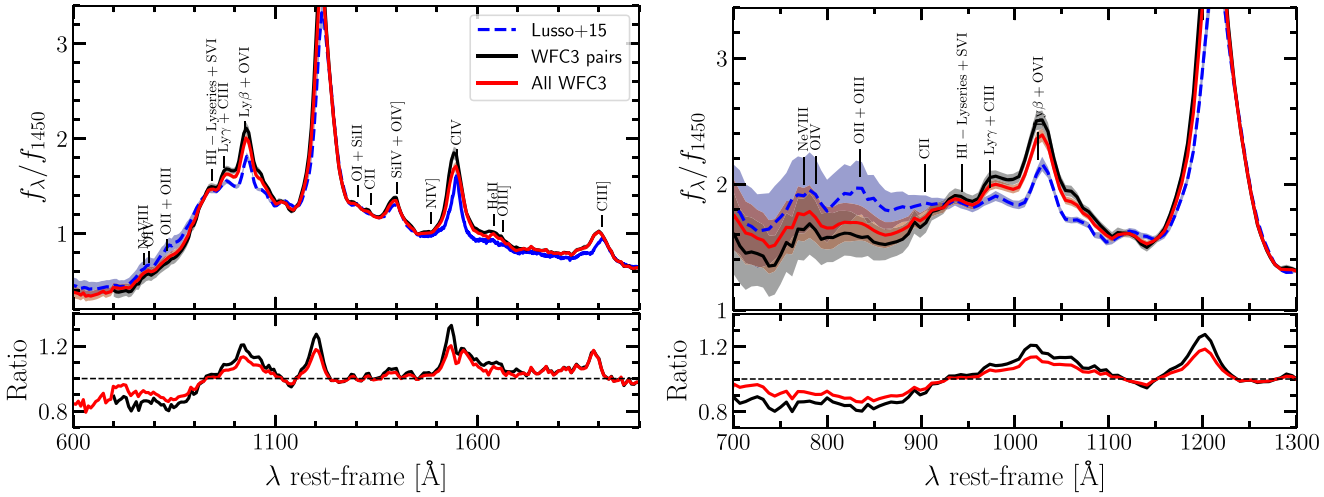

Figure 4. Left panel: mean observed quasar spectrum for the new WFC3 quasar pair sample (94 quasars, black solid line) obtained from 10,000 bootstraps compared to the one obtained from a stack of 53 WFC3 spectra at redshift $z \simeq 2.44$ (L15, blue dashed line). The spectral composite considering all WFC3 quasars (157 objects) is plotted with the green solid line. All spectra are normalized to unit flux at 1450 Å. The new WFC3 to the L15 spectral stack ratio is shown in the bottom panel with the black solid line. We also show the ratio between the stack obtained with the whole WFC3 sample (157 objects) and the L15 stack (green solid line) for completeness. Right panel: zoom-in of the mean IGM-corrected quasar spectrum at short wavelengths with uncertainties from bootstrap (shaded area) for the WFC3 pair sample (black solid line), for the L15 (blue dashed line) sample, and considering all WFC3 quasars (157 objects).

WFC3/UVIS-G280 grism. *HST* observations and reduction procedures are described in detail in O'Meara et al. (2011; see also O'Meara et al. 2013). The O'Meara et al. (2011) survey consists of 53 single quasars selected from SDSS-DR5 with $g^* < 18.5$ mag, with an average redshift of $\langle z \rangle \simeq 2.44$. These data were taken specifically for the scientific goal of surveying the abundance of strong H I Lyman limit absorption features at $z \gtrsim 1.5$. The WFC3/UVIS-G280 spectra utilized in L15 have relatively high S/N (∼20) per pixel down to $\lambda_{\rm obs} \sim 2000$ Å [19] (with an FWHM ∼ 60 Å at $\lambda_{\rm obs} = 2500$ Å). In comparison, our new survey has been designed to characterize the small-scale structure of optically thick gas in the circumgalactic medium (CGM) by observing 54 double sight lines at impact parameters in the range 10–250 kpc (Fumagalli et al. 2014). While both the L15 and the quasar pair sample are selected based on a similar SDSS optical color selection, the pair sample is roughly two magnitudes fainter ($g^* = 18.3$–21.6) and spans a wider redshift range ($1.9 < z < 2.7$, with $\langle z \rangle \simeq 2.3$) than the L15 single quasar sample. Our quasar pair spectra also have by comparison lower S/N on average, with S/N < 10 per pixel down to $\lambda \sim 2000$ Å than the L15 sample.

The spectral quasar composite (not corrected for IGM absorption) obtained with our new WFC3 quasar pair sample (94 objects) is presented in Figure 4 together with the one published by L15 for single quasars. The new WFC3 quasar pair composite is shown as the solid black line, while the resulting uncertainties on the stacked spectrum are plotted with a shaded area.

The shapes of the two composites are similar overall, yet the new quasar pair stack shows (1) a moderate emission line flux excess and (2) a ∼30% decrease in flux at $\lambda = 800$–900 Å with respect to the L15 one. The latter may be due to relatively small differences in the ionizing continua of quasar pairs with respect to single quasars, differences in the environment, or a combination of the two. We will discuss this in detail in Sections 4.1 and 5.

[19] The data generally have S/N exceeding 10 pixel^{-1} at all wavelengths $\lambda_{\rm obs} > 2000$ Å.

Regarding the first point, the observed flux excess can be ascribed to the classical *Baldwin effect*, that is, the anticorrelation between the rest-frame equivalent width (EW) of a broad emission line and the continuum quasar luminosity (Baldwin 1977). This anticorrelation becomes steeper toward higher quasar luminosities and for broad emission lines with higher ionization potentials (Dietrich et al. 2002). Such behavior is also consistent with the shape of the ionizing continuum becoming softer for more luminous quasars (e.g., Malkan & Sargent 1982; Netzer et al. 1992; Zheng & Malkan 1993; Green 1996; Zheng et al. 1997; Lusso et al. 2015).

Finally, we also constructed for completeness the composite considering all of the WFC3 quasars: L15 plus the WFC3 quasars presented here considering lenses and the two field quasars, as well as the projected pair, for a total of 157 sources. For the lenses, we only considered the spectrum with the higher S/N. The resulting stack obtained from 20,000 bootstraps is plotted in Figure 4 with the red solid line. This composite, as expected, has a shape similar to the one resulting from the new WFC3 quasar pair sample, with only a few minor differences in the emission line flux. By including the additional WFC3 single quasars from L15, the S/N at 700 Å of the resulting stack is improved by roughly a factor of two.

3.2. Stack in Redshift Intervals

We further investigate how the spectral shape changes by splitting the new WFC3 quasar pair sample into two almost equally populated redshift bins: 48 quasars for the low-redshift sample ($1.96 \leqslant z \leqslant 2.24$, with a mean $\langle z \rangle \simeq 2.09$), and 46 quasars for the high-redshift sample ($2.26 \leqslant z \leqslant 2.67$, $\langle z \rangle \simeq 2.44$). The resulting composites are presented in Figure 5. Interestingly, the most notable difference between these two stacks is at $\lambda < 912$ Å, where the low-redshift stack shows roughly a factor of two increase in flux compared to the high-redshift one. Given that the higher redshift interval is similar in both source statistics and average redshift with respect to the L15 sample, one may expect to observe similar levels of absorption and shape of the composites. Yet, the

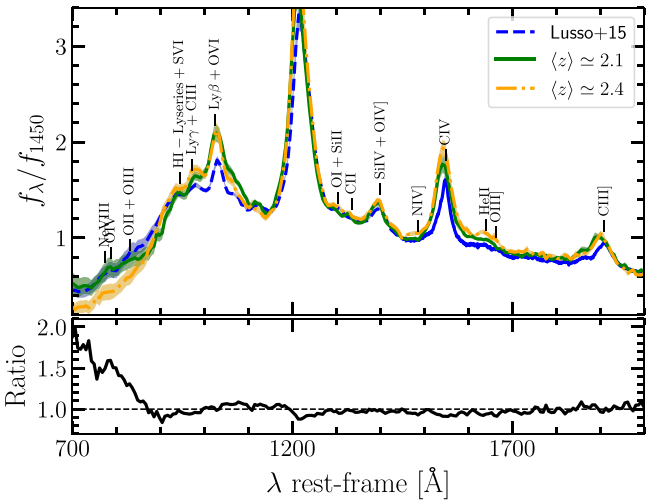

Figure 5. Comparison between the mean observed quasar pair composite (from bootstrap) for the low-redshift (48 quasars, $\langle z \rangle \simeq 2.09$, green solid line) and the high-redshift (46 quasars, $\langle z \rangle \simeq 2.44$, orange dot-dashed line) quasar samples. The WFC3 and SDSS quasar composites by L15 are also shown as a reference. The ratio between the low-z and the high-z stack is shown in the bottom panel.

high-redshift quasar pair composite presents significant absorption (fluxes are dimmed by up to a factor of two at 700 Å) compared to the L15 one. On the other hand, the level of absorption of the pair composite in the low-z stack at $z \sim 2.09$ is overall similar to the L15 one, which is, however, at an average redshift of $\langle z \rangle \simeq 2.44$.

4. IGM Absorption Correction

Absorption from intergalactic H I attenuates the quasar flux at wavelengths blueward of Lyα, both in the Lyman series (creating the so-called Lyman forest) and in the Lyman continuum at rest, $\lambda < 912$ Å (e.g., Moller & Jakobsen 1990). The significant abundance of neutral gas at $z > 2$ is clear in our average quasar spectrum shown in the left panel of Figure 4.

To recover the IGM-corrected quasar emission, we considered the IGM transmission functions (T_λ) published by Prochaska et al. (2014, P14 and references therein) along with their uncertainties. These functions have been computed through a cubic Hermite spline model, which describes the H I absorber distribution function that, in turn, depends upon both redshift and column density ($f(N_{\rm H\,I}, z) = \partial^2 n/(\partial N_{\rm H\,I}\partial z)$). P14 then performed a Monte Carlo Markov chain (MCMC) analysis of existing constraints on $f(N_{\rm H\,I}, z)$ to derive the posterior probability distribution functions of seven spline points spaced at irregular logarithmic intervals in the range $N_{\rm H\,I} = 10^{12}$–10^{22} cm^{-2}.

Here we consider 10,000 realizations of $f(N_{\rm H\,I}, z)$ and calculated T_λ in the observed wavelength range with a semianalytic technique (see Figure 3 in L15). This modeling assumes that the H I forest is composed of discrete "lines" with Doppler parameter $b = 24$ km s^{-1} and that the normalization of $f(N_{\rm H\,I}, z)$ evolves as $(1+z)^{2.0}$ (Prochaska et al. 2009). This redshift evolution is somewhat faster than what has been found at lower redshifts. Danforth et al. (2016) presented a COS survey of Lyα forest absorbers ($\log N_{\rm H\,I} > 13$) at $z < 0.47$, finding $\gamma = 1.24 \pm 0.04$, while Shull et al. (2017) found $\gamma = 1.14 \pm 0.89$ from a survey of LLSs and partial LLSs ($15.0 \leqslant \log N_{\rm H\,I} \leqslant 17.5$) at $0.24 < z < 0.48$. From an *HST* survey extended to higher redshifts, Ribaudo et al. (2011) obtained $\gamma = 1.19 \pm 0.56$ for LLSs with $\tau_{\rm LLS} \geqslant 1$, also including partial LLSs, at $0.25 \leqslant z \leqslant 2.59$ ($\gamma = 1.33 \pm 0.61$ with $\tau_{\rm LLS} \geqslant 2$). Our assumed redshift evolution is somewhat consistent, within the uncertainties, with the γ values obtained in high-redshift surveys, and it is a reasonable value for the Lyα forest of quasars at $z \simeq 2$, as it implies an increasing transmission for the lower-redshift Lyman series (Prochaska et al. 2009, 2014). Opacity due to metal line transitions was ignored since they contribute negligibly to the total absorption in the Lyman continuum.

Table 2
WFC3 Stacked Spectrum Corrected for IGM Absorption

λ[a]	$f_{\lambda,\rm All}$[b] All WFC3	$\sigma(f_{\lambda,\rm All})$[c] (157 quasars)	$f_{\lambda,\rm pairs}$ Pairs only	$\sigma(f_{\lambda,\rm pairs})$ (94 quasars)
700.955	1.752	0.279	1.603	0.323
707.144	1.683	0.262	1.508	0.297
713.334	1.611	0.250	1.451	0.291
719.524	1.598	0.238	1.460	0.274
725.713	1.569	0.225	1.448	0.256
731.903	1.553	0.220	1.429	0.255
738.093	1.499	0.213	1.348	0.250
744.282	1.514	0.208	1.355	0.244
750.472	1.584	0.208	1.436	0.232

Notes.
[a] Rest-frame wavelength in angstrom.
[b] Mean IGM-corrected flux per Å normalized to the flux at 1450 Å.
[c] Flux uncertainties from our bootstrap analysis (see Section 4).
(This table is available in its entirety in machine-readable form.)

The technique we followed is similar to the one described in L15. We briefly summarize the main steps below:

1. We first generate a set of 20,000 mock quasar stacks, following the same procedure as in Section 3, by drawing randomly from the 94 quasar spectra to assess sample variance (allowing for duplications).
2. We then randomly draw one IGM transmission function from our suite of 10,000. We smoothed this to the WFC3 grism resolution (five pixels), and we resampled the transmission function onto the rest-frame wavelength grid of our stacked quasar spectrum. This is repeated for each mock quasar stack.
3. We divide the observed spectral flux ($f_{\lambda,\rm obs}$) by the IGM transmission curve, $f_{\lambda,\rm corr} = f_{\lambda,\rm obs}/T_\lambda$.
4. The 20,000 mock stacks corrected from IGM absorption are then averaged to produce the stacked spectrum (normalized to unity at $\lambda = 1450$ Å).
5. The uncertainties on the corrected WFC3 stacked spectrum are estimated from the dispersion of these 20,000 mock stacks.

The resulting stack for our WFC3 quasar pair sample is shown in the right panel of Figure 4, along with its 1σ uncertainties and the WFC3 composite published by L15 as a comparison. The stacked spectra show somewhat similar shapes, with a softening at wavelengths $\lambda < 912$ Å and several (mostly blended) emission lines.

The average IGM-corrected WFC3 composites for the full WFC3 quasar sample (157 quasars) and for the pairs only (94 quasars) are tabulated in Table 2.

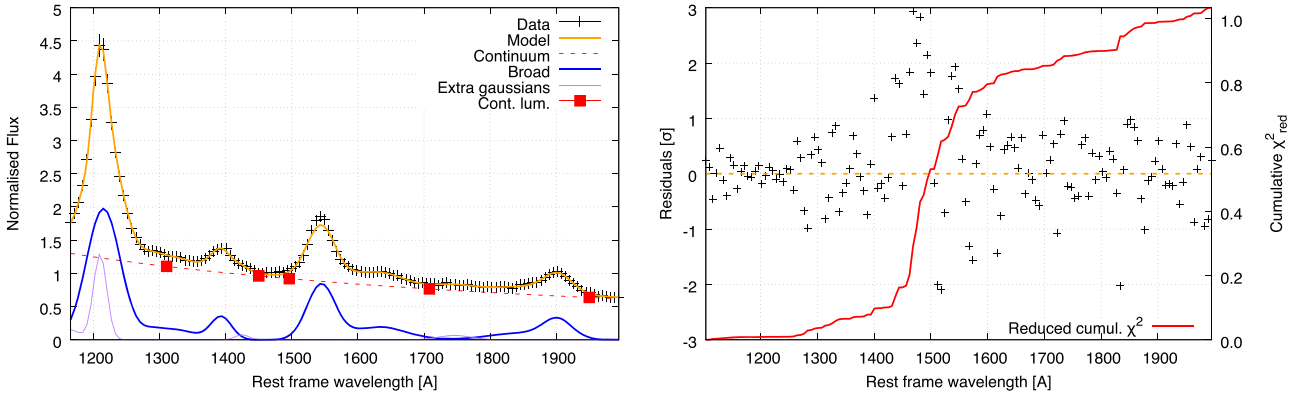

Figure 6. Left panel: QSFit model (orange line) of the average spectrum of the 94 quasars normalized at 1450 Å. The individual components in the QSFit model are the continuum component (dashed red line); the sum of all broad emission line components is shown with a blue line. The sum of all "Extra Gaussian" lines (features not fitted with any known emission line) is shown with a purple solid line. The red squares are the continuum luminosity estimated by QSFit (see Section 4.1 for details). Right panel: residuals (data model) in units of 1σ uncertainties in the data (black cross symbol) and the cumulative reduced χ^2 (red line, values on the right-hand axis).

4.1. Spectral Fit

We measured the properties of the most prominent emission lines and the spectral continuum by employing QSFit (Quasar Spectral Fitting package; Calderone et al. 2017), which automatically performs the analysis of quasar spectra. This software provides, among other parameters, FWHM values, velocity offsets, and EWs of a number of emission lines. QSFit fits all of the components simultaneously considering a single power law to describe the quasar continuum over the entire (rest-frame) wavelength coverage. We defer the interested reader to Calderone et al. (2017) for details; here we briefly summarize the main features of this software that are relevant for our analysis. We fitted the broad component of several emission lines such as Lyα, Si IV, C IV, and the semiforbidden line of C III], as well as a combination of templates for the optical and UV iron emission (Vestergaard & Wilkes 2001; Véron-Cetty et al. 2004). We also considered a list of weaker lines that are not identified by QSFit (i.e., lines not associated with any known line; Section 2.7 in Calderone et al. 2017). These additional components account for asymmetric profiles in known emission lines.

Lines and blends at $\lambda < 1216$ Å from high-ionization states, such as O IV 608, O V 630, N III 685, O III 702, Ne VIII+O IV 772, and Lyγ+C III] 873, may also be present, but it is impossible to reliably measure their strengths given the noise in our stacked spectrum at blue wavelengths. We thus fit our quasar composite only at $\lambda > 1100$ Å. At the redshift and wavelength ranges probed by our WFC3 sample, the emission from the hosting galaxies and the Balmer continuum are negligible; we thus neglected both components in the fit.

Figure 6 (left panel) shows the rest-frame stacked spectrum for the 94 quasars extending from 1100 to 2000 Å and the power-law fit to the continuum of the form $f_\lambda \propto \lambda^{\alpha_\lambda}$, where the best-fit power-law index is $\alpha_\nu = -0.61 \pm 0.08$[20] (dot-dashed line), in good agreement with previous works in the literature. A summary of the spectral properties (i.e., FWHM, velocity offset, and EWs) for the most prominent lines with no quality flag raised (i.e., "good," whose quality flag is 0) is provided in Table 3.

[20] In the following we will refer to α_ν only. The relation between the fluxes in wavelength, $f_\lambda \propto \lambda^{\alpha_\lambda}$, and frequencies, $f_\nu \propto \nu^{\alpha_\nu}$, is $\alpha_\nu = -(2 + \alpha_\lambda)$.

Table 3
Spectral Properties of the WFC3 Quasar Pair Composites

Line	λ (Å)	FWHM[a] (km s^{-1})	$v_{\rm obs}$[b] (km s^{-1})	EW[a] (Å)
		pairs		
Lyα	1215.7	10834.0 ± 904.0	1518.2 ± 175.2	68.3 ± 4.6
Si IV	1399.8	8220.7 ± 953.1	1356.2 ± 284.8	13.3 ± 3.5
C IV	1549.48	8483.9 ± 225.5	1067.7 ± 105.2	50.0 ± 2.0
C III]	1908.734	8405.5 ± 398.4	1356.3 ± 182.2	22.0 ± 6.7
		L15		
Lyα	1215.7	11848.0 ± 804.7	148.1 ± 125.2	57.3 ± 3.2
Si IV	1399.8	8428.0 ± 782.2	568.0 ± 258.1	12.3 ± 0.7
C IV	1549.5	5857.2 ± 354.7	301.8 ± 72.7	19.2 ± 4.6
C III]	1908.7	7291.5 ± 151.7	−50.4 ± 63.0	10.0 ± 0.3
		Additional Lines		
He II	1640.4	14912.0 ± 892.1	1486.8 ± 301.2	9.5 ± 0.7
O III	1665.8	3534.4 ± 913.4	−860.1 ± 288.4	0.65 ± 0.3

Notes.
[a] FWHM and equivalent widths of the emission lines in the WFC3 stack normalized at 1450 Å. Only the broad component of the emission line is reported.
[b] Velocity offset with respect to the reference wavelength (only broad component).

To compare these findings with the ones of L15, we refitted their composite (WFC3 + SDSS) for single quasars using QSFIT with the same setup. We find the same quasar continuum slope of $\alpha_\nu = -0.61 \pm 0.10$, while the FWHM, $v_{\rm obs}$, and EW are reported in Table 3.

The ionizing slope is estimated by modeling continuum +lines with a simple single power law in a similar fashion as done by L15. We computed the best-fit slope of the composite at $\lambda < 912$ Å results from a χ^2 minimization in each bootstrap realization, as described in Section 4. The final value we quote for the spectral slope (along with the 1σ uncertainties) is estimated from the mean (and standard deviation) of all the bootstrap realizations. The resulting ionizing slope is $\alpha_{\rm ion} = -2.48 \pm 0.77$. Figure 7 presents a zoom-in of the ionizing part of the composite with the resulting best fit. We caution that, given the low WFC3 resolution and the high level of noise in the ionizing region, we cannot identify weak lines that should be present at $\lambda < 912$ Å, including Ne VIII 775,

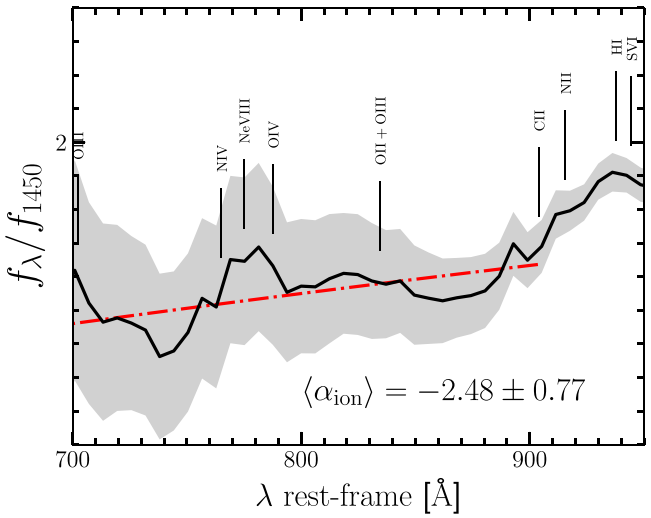

Figure 7. Ionizing region of the average spectrum normalized at 1450 Å (700–912 Å) for the 94 quasars. The dashed line is the power-law continuum +lines obtained by fitting the rest-frame composite at $\lambda < 912$ Å.

O IV 787.7, O II+O III 834.5, and Lyγ+C III 873. Blended lines from high-ionization states such as O IV 608, O V 630, N III 685, and O III 702 (fundamental diagnostics for studying the physical conditions of broad emission line regions) may also be present, although it is impossible to reliably measure their strengths. For example, the "dip" at $\lambda \simeq 730$–750 Å could also be a line-free region instead of a trough. However, the same dip is observed in the geometric mean (regarded as the better characterization of the AGN composite) by S14 (see the top panel of their Figure 5), and the stack has a ionizing slope of -1.41 ± 0.15, while this dip disappears in their median (bottom panel of their Figure 5, showing a slope of -1.32 ± 0.15). This further highlights the challenge in estimating the ionizing slope in quasar spectra. Our ionizing slope of the spectral fit shown in Figure 7, although uncertain, should only be considered representative of the combined contribution of both continuum and emission lines of quasars at $z > 2$ given the IGM transmission functions employed (possible caveats are discussed in Section 4.2).

We also computed the nonionizing and ionizing spectral slopes by considering the IGM-corrected spectral stack of the combined WFC3 sample from our previous survey (i.e., O11, O13, L15; 53 quasars) and the whole *HST* quasar sample from our new WFC3 program (104 quasars), totaling 157 quasar spectra. We find spectral slopes of $\alpha_\nu = -0.52 \pm 0.04$ and $\alpha_{\rm ion} = -1.98 \pm 0.50$ for the nonionizing and ionizing parts of the spectrum, respectively, in statistical agreement with the values obtained considering only the WFC3 quasar pair sample.

As discussed by L15, our analysis supports the results that a single power law does not seem to be a satisfactory description of the region below 912 Å, where the continuum exhibits a break with a flatter (softer) spectrum (see also Telfer et al. 2002). The shape of our new WFC3 stacks presents a 20% flux decrement around 912 Å and a very faint O II+O IIIλ834.5Å blend. Additionally, it is not trivial to interpret the feature at ~730 Å as intrinsic continuum or absorption. Therefore, given the poor spectral resolution and the difficulties in fitting the ionizing spectral region, we refrain from employing more complicated models.

4.2. Caveat on the IGM Transmission Function Employed

The new WFC3 spectral stack (see Figures 4 and 7), corrected for the IGM absorption following the procedure outlined at the beginning of this section, implicitly assumes that our employed T_λ functions are, on average, representative of the IGM of quasar pairs. In other words, the environment of quasar pairs is not expected to be statistically different from that of single quasars. Nonetheless, the T_λ function critically depends upon the parameterization of $f(N_{\rm H\,I}, z)$ (Madau 1995; Meiksin 2006; Inoue et al. 2014), and its statistical nature is due to the stochasticity of LLSs (Bershady et al. 1999; Inoue & Iwata 2008; Worseck & Prochaska 2011). Our approach takes into account the stochasticity of Lyman limit absorption (Worseck & Prochaska 2011), so this is the best way to correct for Lyman series and Lyman continuum absorption of low-column-density absorbers that cannot be identified and corrected by eye. In addition, LLSs could perhaps be masked by the low spectral resolution of WFC3, which prevents an unambiguous identification of weak partial LLSs in individual spectra without knowledge of the underlying quasar continuum.

The new WFC3 quasar pair spectral composite (with $\alpha_\nu \simeq -2.5 \pm 0.8$) is thus representative of the intrinsic shape (which we argue is in the range $\alpha_\nu \simeq -1.4, -1.7$) plus any additional contribution of absorption associated with the quasar pair environment, which is not captured by our T_λ functions. To investigate this further, in the following sections we will focus our attention on the ionizing region of the spectral composite to provide a better modeling of the IGM properties in proximity to these pairs.

5. The Mean Free Path

The most notable absorption features in quasar spectra are optically thick absorption line systems, namely LLSs and damped Lyα absorbers (DLAs). These systems have a higher neutral hydrogen fraction than the IGM and have column densities of $N_{\rm H\,I} > 10^{17.2}$ cm^{-2} (i.e., they are optically thick to Lyman continuum photons). They play a major role in modulating the intensity of the extragalactic UV background and in the determination of the mean free path to ionizing photons in the IGM (e.g., Rauch et al. 1997; Fardal et al. 1998; Shull et al. 1999; Faucher-Giguère et al. 2008, 2009; Haardt & Madau 2012).

Our previous analysis has focused on the spectral properties of the quasar pairs once corrected for an average IGM absorption. We now assess more quantitatively the properties of the UV composite at <910 Å to investigate whether the quasar pair sample displays differences compared to single quasars, which could be ascribed to a different environment or a different ionization state of the IGM near these quasars. The first measurement we perform to this end is quantifying the mean free path of ionizing photons.

5.1. Formalism

To estimate the mean free path to ionizing radiation, $\lambda_{\rm mfp}^{912}$, we consider and review the model presented by O'Meara et al. (2013, O13 hereafter, see also O'Meara et al. 2011; Worseck & Prochaska 2011; Fumagalli et al. 2013; Prochaska et al. 2014; Worseck et al. 2014). The observed stacked quasar spectral energy distribution (SED) blueward of Lyα (i.e.,

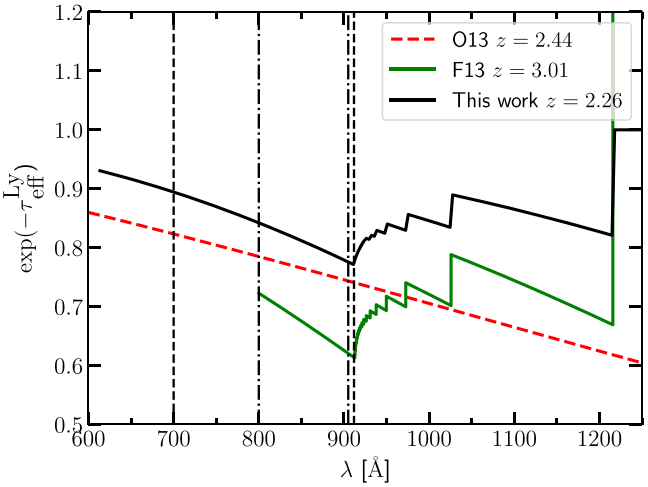

Figure 8. Our adopted Lyman series opacity as defined in Equation (4), where the employed $f(N_{\rm H\,I}, z)$ function is taken from Prochaska et al. (2014) and extrapolated at $z_{\rm qso} \simeq 2.26$ for a fixed Doppler parameter $b = 24$ km s^{-1} (black solid line). The green line represents $\tau_{\rm eff}^{\rm Ly}$ for a redshift $z \simeq 3$ (Fumagalli et al. 2013), while the red dashed line is the best-fit Lyman series opacity obtained by O13 given Equation (2), with $\tau_{\rm eff}^{\rm Ly}(\lambda_{912}) = 0.3$ and $\gamma_\tau = 1.64$. The vertical dashed and dot-dashed lines represent the wavelength ranges 700–912.76 Å and 800–905 Å, respectively.

$\lambda < 1216$ Å) can be modeled as

$$f_{\lambda,\rm obs} = a f_{\lambda,\rm SED}\lambda^{-\alpha}\exp(-\tau_{\lambda,\rm eff}), \quad (1)$$

where the term $af_{\lambda,\rm SED}\lambda^{-\alpha}$ accounts for the intrinsic quasar ionizing continuum ($f_{\lambda,\rm intr}$), and it will be discussed in detail in Section 5.2. The $\tau_{\lambda,\rm eff}$ parameter is the effective optical depth due to intervening absorbers and includes the contribution of absorption in the hydrogen Lyman series ($\tau_{\rm eff}^{\rm Ly}$) and the Lyman continuum ($\tau_{\rm eff}^{\rm LL}$) at $\lambda < 912$ Å (i.e., $\tau_{\lambda,\rm eff} = \tau_{\rm eff}^{\rm Ly} + \tau_{\rm eff}^{\rm LL}$). The redshift evolution for $\tau_{\rm eff}^{\rm Ly}$ is usually defined as

$$\tau_{\rm eff}^{\rm Ly}(\lambda) = \tau_{\rm eff}^{\rm Ly}(\lambda_{912})\left(\frac{1+z_{912}}{1+z_{\rm qso}}\right)^{\gamma_\tau}, \quad (2)$$

where z_{912} is the redshift at which a photon emitted at the redshift of the quasar ($z_{\rm qso}$) is absorbed at the Lyman limit:

$$z_{912} = \lambda(1+z_{\rm qso})/\lambda_{912} - 1. \quad (3)$$

As already discussed by Fumagalli et al. (2013) and Worseck & Prochaska (2011), one could consider both $\tau_{\rm eff}^{\rm Ly}(\lambda_{912})$ and γ_τ as free parameters, but the data between 700 and 912 Å do not constrain them independently. To account for the Lyman series opacity, we have thus estimated $\tau_{\rm eff}^{\rm Ly}$ numerically as

$$\tau_{\rm eff}^{\rm Ly}(z) = \sum_{n=1}^{\infty}\int\int\int_{z}^{z_{\rm qso}} f(N_{\rm H\,I}, z', b)\exp(-\tau_\nu^n)dN_{\rm H\,I}dz'db, \quad (4)$$

where τ_ν is the optical depth due to the incidence of the Ly series ($n = 1, 2, 3, \ldots$ corresponds to Lyα, Lyβ, Lyγ, etc.; Madau et al. 1999), and $f(N_{\rm H\,I}, z)$ is the column density distribution function from Prochaska et al. (2014). We have fixed the Doppler parameter b for the Ly series to 24 km s^{-1} and $z_{\rm qso}$ to the average redshift of the quasar sample ($z_{\rm qso} \simeq 2.26$). The resulting Lyman series opacity is plotted in Figure 8. As a comparison, we also plotted the best-fit Lyman series opacity obtained by O13 given Equation (2), with $\tau_{\rm eff}^{\rm Ly}(\lambda_{912}) = 0.3$ and $\gamma_\tau = 1.64$ (see their Equation (4) and Table 7), and the one employed by Fumagalli et al. (2013) for $z \simeq 3$ quasars. The characteristic sawtooth behavior is due to the incidence of the Ly series lines (τ_ν), while the shape at wavelengths bluer than 912 Å depends upon the adopted $f(N_{\rm H\,I}, z)$. Such a correction is in any case minor compared to the Lyman limit opacity, of the order of ~10%–15% in the wavelength range of interest.

The last parameter we need to model is the Lyman limit optical depth, which is set by the opacity $\kappa^{\rm LL}$ seen at each redshift by the ionizing photons emitted at $\lambda < 912$ Å over a path length r from the quasar redshift to z:

$$\tau_{\rm eff}^{\rm LL}(\lambda) = \int_0^r \kappa^{\rm LL}(r', \lambda)dr'. \quad (5)$$

Following Fumagalli et al. (2013; see their Section 4), the opacity $\kappa^{\rm LL}(r, \lambda)$ can be rewritten as a function of redshift:

$$\kappa^{\rm LL}(r, \lambda) \simeq \kappa^{\rm LL}(z) = \kappa_{912}^{\rm LL}(z)\left(\frac{1+z}{1+z_{\rm qso}}\right)^{-2.75}, \quad (6)$$

which is defined by the product of the redshift-dependent opacity $\kappa_{912}^{\rm LL}(z_{\rm qso})$ and the H I photoionization cross section ($\sigma_{\rm ph} \propto \lambda^{2.75}$). The dependence of $\kappa_{912}^{\rm LL}(z)$ on redshift can be parameterized as follows:

$$\kappa_{912}^{\rm LL}(z) = \kappa_{912}^{\rm LL}(z_{\rm qso})\left(\frac{1+z}{1+z_{\rm qso}}\right)^{\gamma_\kappa}, \quad (7)$$

but since $\kappa_{912}^{\rm LL}(z)$ is only weakly dependent on redshift ($\gamma_\kappa \simeq 0.4$ at $z \simeq 2.4$, O13), we assume $\gamma_\kappa = 0$ for our analysis. For a given cosmology,

$$\frac{dr}{dz} = \frac{c}{H_0(1+z)\sqrt{\Omega_{\rm M}(1+z)^3 + \Omega_\Lambda}}, \quad (8)$$

where we neglect the contribution of Ω_Λ given the redshift range probed by our quasar sample, resulting in error on the order of 3%–5% in our measurement. By combining the above equations, we can now define the final expression for the Lyman limit opacity as

$$\tau_{\rm eff}^{\rm LL} = \frac{c}{H_0\sqrt{\Omega_{\rm M}}}(1+z_{912})^{2.75}\kappa_{912}^{\rm LL}(z_{\rm qso})\int_{z_{912}}^{z_{\rm qso}}(1+z')^{-5.25}dz'. \quad (9)$$

The final model for the normalized observed quasar SED is thus constructed by combining Equations (4) and (9) in (1).

5.2. The Intrinsic Quasar SED

To quantify the "extra" absorption observed in the quasar pair composite, we need to model the shape of the intrinsic quasar SED. This is a key assumption in our estimate of the mean free path and a necessary step in order to probe the foreground IGM. Previous works in the literature have found very similar slopes in the 1200–2000 Å wavelength range, with spectral indexes roughly around $\alpha_\nu \simeq -0.61, -0.83$ (e.g., L15; Stevans et al. 2014), while the situation changes at much shorter wavelengths (e.g., the rest-frame range

500–1200 Å), where the slope may vary significantly, from $\alpha_\nu \simeq -0.56, -0.72$ (Scott et al. 2004; Tilton et al. 2016), to $\alpha_\nu \simeq -1.41, -1.70$ (Shull et al. 2012; Stevans et al. 2014; L15).

However, given the similarity of the redshift range between our quasar sample and the one presented by L15, we assume that the underlying intrinsic quasar SED is the L15 (corrected for IGM absorption) modulated with a power law $\alpha = 0.3$, that is, $\alpha_\nu = -1.7$; we assumed that the intrinsic continuum slopes are the same for both pairs and single quasars (the differences arise in the large-scale environment):

$$f_{\lambda,\mathrm{intr}} = a f_{\lambda,\mathrm{L15}} \left(\frac{\lambda}{1450\ \text{Å}} \right)^{-0.3}, \quad (10)$$

where a allows for an offset between the assumed intrinsic SED and the WFC3 composite, which is a free parameter. Even though the quasar SED is normalized to 1450 Å, there may be some nontrivial difference in the flux measurement or emission line strength. Given the different nature of our sample (i.e., ∼90% are close quasar pairs versus single field quasars), and the fact that the observed SED seems to show a mild level of absorption at ∼800–850 Å (see Figure 4), we will discuss how our results change if we assume different intrinsic quasar SEDs in the following section.

5.3. Estimating the Mean Free Path

We apply the formalism described in Section 5 to the observed WFC3 composite to obtain an estimate of $\lambda_{\mathrm{mfp}}^{912}$. We proceed by first building a set of stacked spectra with a standard bootstrap technique (allowing for repetition). For each quasar stack, we then applied a maximum-likelihood analysis in the wavelength interval 700–911.76 Å where the free parameters are a and $\kappa_{912}^{\mathrm{LL}}(z_{\mathrm{qso}})$. The wavelength range for the model fit is chosen to be consistent with the one defined by O13 for comparison purposes; nonetheless, we have also investigated how the slope changes if we consider a more conservative (narrower) wavelength range, 800–905 Å. The higher wavelength is chosen to avoid the quasar proximity region at >905 Å, while the lower bound is set to avoid the possible contribution of noisy data (Fumagalli et al. 2013; Worseck et al. 2014).

Given the wide range of ionizing spectral slopes published in the literature, we have also further examined the dependence of $\lambda_{\mathrm{mfp}}^{912}$ on the assumed intrinsic spectral shape. As our quasar pair sample is at $z > 2$, one possibility is to consider the composite SED published by Telfer et al. (2002). However, as already discussed by L15 and Scott et al. (2004), the IGM correction considered by Telfer et al. (2002) is basically negligible at $\lambda \leqslant 1200$ Å, even if $z > 2$ quasars are the main contributors at these wavelengths. The more recent spectral composites published by Shull et al. (2012) and S14 are identical, with ionizing spectral slopes (500–1000 Å) of $\alpha_\nu = -1.41 \pm 0.21$ and -1.41 ± 0.15, respectively. These slope values are more precise than the ones we can compute from our WFC3 data, as they have been estimated by taking advantage of the higher spectral resolution of COS, which allows the authors to fit the local continua (correcting for identified LLSs and pLLSs), taking into account the contribution of quasar emission lines (see also Shull et al. 2017). The S14 spectral stack (covering the rest-frame range 475–1875 Å) has been obtained from 159 AGNs at redshifts $0.001 < z < 1.476$ (with an average redshift of $\langle z \rangle = 0.34$) and probes both lower redshifts and optical magnitudes (see Figure 1) with respect to the objects analyzed here. Nonetheless, given their composite is at much higher resolution than our WFC3 one and is directly corrected for both LLSs and pLLSs, which we do statistically, we decided to consider also the intrinsic quasar SED published by S14. We scaled and tilted the COS composite considering their observed spectral slope at $\lambda < 912$ Å as

$$f_{\lambda,\mathrm{intr}} = a f_{\lambda,\mathrm{S14}} \left(\frac{\lambda}{1450\ \text{Å}} \right)^{-0.6}. \quad (11)$$

The COS stack is also rebinned to the dispersion solution of our stacked spectrum and smoothed to the WFC3 spectral resolution. The best estimate of the mean free path ($\lambda_{\mathrm{mfp}}^{912} \propto 1/\kappa_{912}^{\mathrm{LL}}(z_{\mathrm{qso}})$) is derived by the mean (median) of 15,000 different realizations along with its uncertainties.

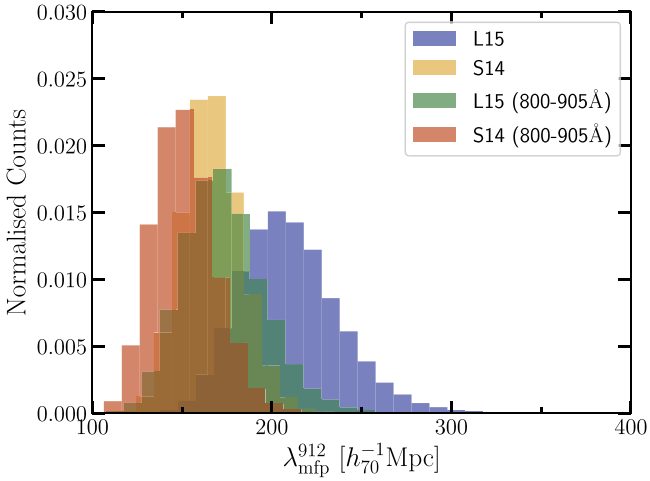

Figure 9. Distributions of the best-fit $\lambda_{\mathrm{mfp}}^{912}$ values derived by modeling the 700–911.76 Å wavelength range of 15,000 composite spectra via the bootstrap technique described in Section 5. We considered two different models for the intrinsic quasar SED: the IGM-corrected L15 spectral stack (blue histogram) and the Stevans et al. (2014) composite (orange histogram). The same analysis has also been performed over a narrower wavelength range (i.e., 800–905 Å).

The normalized distributions of the best-fit $\lambda_{\mathrm{mfp}}^{912}$ values for the 15,000 different realizations of our quasar pair sample, computed by assuming the L15 and S14 stacks as the underlying continua and the 700–911.76 Å and 800–905 Å wavelength intervals, are shown in Figure 9. The 1σ and 2σ contours of the best $\lambda_{\mathrm{mfp}}^{912}$ and a values resulting from our maximum-likelihood analysis are presented in Figure 10. The $\lambda_{\mathrm{mfp}}^{912}$ distributions show a large dispersion, with the one obtained by assuming the S14 SED and the narrow wavelength interval being the one probing the smaller $\lambda_{\mathrm{mfp}}^{912}$ values. Nonetheless, they are all consistent within the 1.5σ level. A summary of the best-fit a and $\lambda_{\mathrm{mfp}}^{912}$ values is provided in Table 4.

The best-fit models are shown in Figure 11. The left and right panels are obtained by fitting the observed quasar pair composite in [700, 911.76] Å and [800, 905] Å, respectively, while the top and bottom panels present our findings by assuming the IGM-corrected L15 and the S14 composites as the underlying intrinsic quasar SED. The purple curve shows

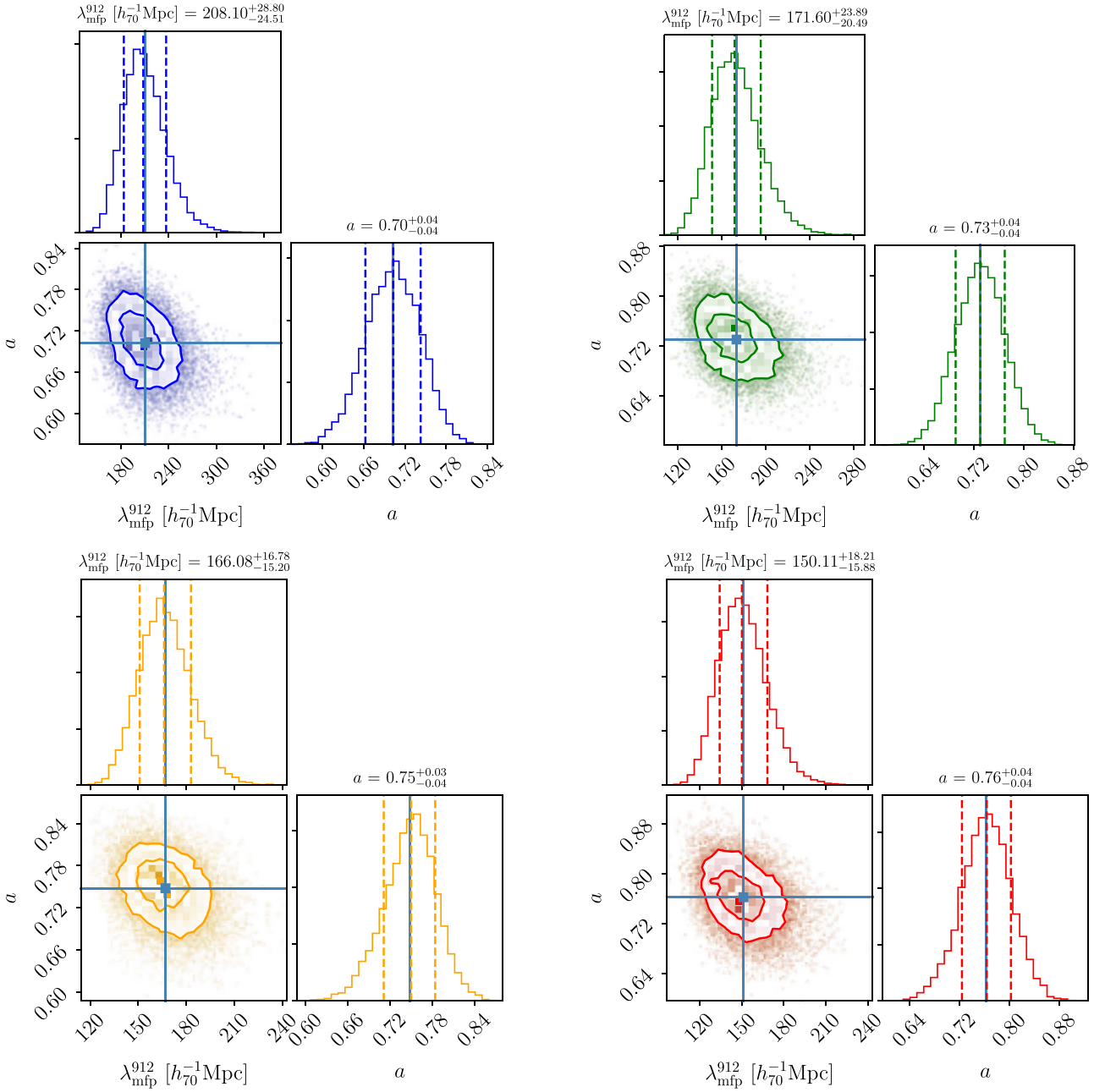

Figure 10. The 1σ and 2σ contours of the best $\lambda_{\rm mfp}^{912}$ and a parameters estimated from 15,000 bootstraps where the analysis has been performed considering both the 700–911.76 Å (left panels) and 800–905 Å wavelength ranges (right panels). The median, 16th, and 84th percentiles are shown on top of the histograms. The mean is shown as a solid line. Top panels: The assumed intrinsic quasar SED is the IGM-corrected L15 spectral stack. Bottom panels: results considering the tilted Stevans et al. (2014) COS quasar composite instead.

Table 4
Mean $\lambda_{\rm mfp}^{912}$ Values from the Analysis of the Quasar Pair WFC3 Sample

SED Model	$\langle\lambda_{\rm mfp}^{912}\rangle$ (h_{70}^{-1} Mpc)	a
L15 (700–911.76 Å)	210.4 ± 27.4	0.70 ± 0.04
S14 (700–911.76 Å)	166.9 ± 16.2	0.75 ± 0.04
L15 (800–905 Å)	173.4 ± 22.7	0.73 ± 0.04
S14 (800–905 Å)	151.3 ± 17.3	0.76 ± 0.04
Low-z sample		
L15 (700–911.76 Å)	314.5 ± 64.9	0.64 ± 0.05
High-z sample		
L15 (700–911.76 Å)	140.7 ± 20.2	0.81 ± 0.06

the best estimate of the intrinsic quasar continuum ($f_{\lambda,\rm intr}$), that is, the scaled and tilted L15 and S14 spectra as defined in Equation (10). The solid red curve represents the complete model, which includes both $\tau_{\rm eff}^{\rm Ly}$ and $\tau_{\rm eff}^{\rm LL}$ in the rest-frame wavelength range considered.

The quasar SED defined in Equation (11) seems to be a better representation of the observed WFC3 stack, which is probably mainly due to the lower contribution of the O II +O IIIλ834.5Å blend (see Figure 4). Yet, in the 800–905 Å interval, the extrapolation of the model to bluer wavelengths clearly shows that it significantly underpredicts the observed quasar flux. We thus consider the SED that includes the broader wavelength range as the most representative.

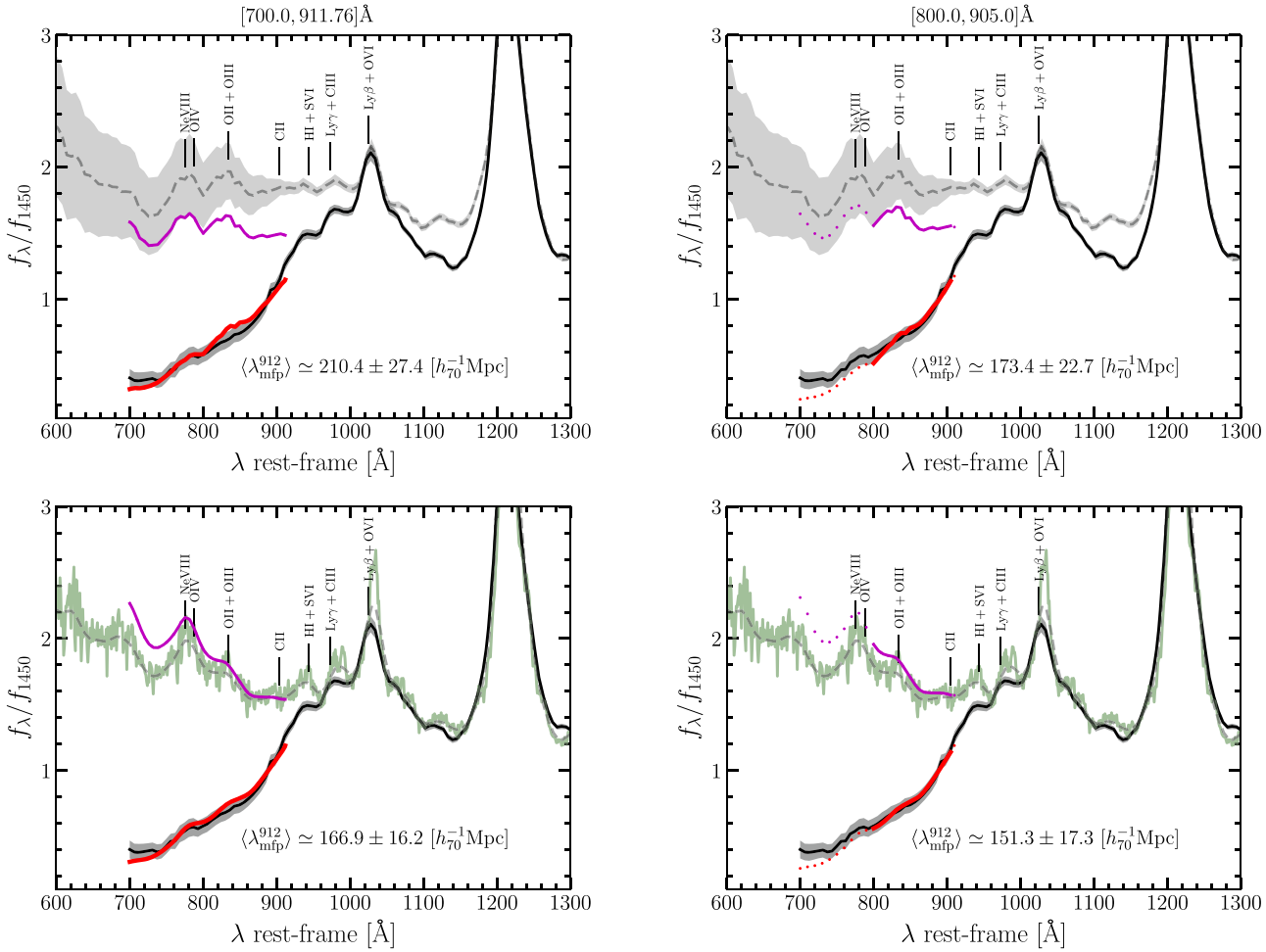

Figure 11. The left and right panels are obtained by fitting the observed quasar pair composite in [700, 911.76] Å and [800, 905] Å, respectively (both ranges are shown on top of the figure). Top panels: The black solid line is the observed WFC3 quasar pair composite, normalized to unity at $\lambda = 1450$ Å. The dashed curve is the IGM-corrected quasar stack by L15 assumed to be the underlying intrinsic quasar SED. The purple curve shows the best estimate of the intrinsic quasar continuum ($f_{\lambda,\rm intr}$), that is, the scaled and tilted L15 spectrum as in Equation (10), where the best-fit a value is provided in Table 4. The solid red curve is the complete model that includes both $\tau_{\rm eff}^{\rm Ly}$ and $\tau_{\rm eff}^{\rm LL}$. The dotted curve (only shown for completeness) represents the region of the spectra (purple: intrinsic assumed spectrum, red: model) that is not taken into account in our fitting procedure in the case of [800, 905] Å. Bottom panels: same as above. The green curve represents the Stevans et al. (2014) quasar composite, where the dashed line is the COS stack rebinned to the dispersion solution of our WFC3 stacked spectrum and smoothed to the WFC3 spectral resolution.

Overall, we find that the $\lambda_{\rm mfp}^{912}$ measurements are all consistent within the 1σ level, with the ones obtained by making use of the tilted Stevans et al. composite predicting slightly steeper intrinsic quasar SEDs at $\lambda < 912$ Å ($\alpha_\nu \simeq -1.41$). We caution that the $\lambda_{\rm mfp}^{912}$ values we found are sensitive to the adopted underlying continuum as well as the contribution of prominent emission lines. Given the results of our analysis, we cannot favor a scenario for quasar pairs having a different ionizing continuum with respect to single quasars in a similar redshift range. We thus argue that the most representative $\lambda_{\rm mfp}^{912}$ estimate ranges between 167 and 210 h_{70}^{-1} Mpc.

As a comparison, the value of the mean free path obtained by O13 for the WFC3 sample of single quasars is $\lambda_{\rm mfp}^{912} \simeq 242 \pm 42\ h_{70}^{-1}$ Mpc (Prochaska et al. 2014), which is in good agreement with our findings within the uncertainties. We stress here that the formalism considered by O13 for the $\lambda_{\rm mfp}^{912}$ measurement is rather different from ours (see their Section 5). Our adopted Lyman series opacity is a factor of ∼12% lower than O13 (see Figure 8), and O13 considered the Telfer et al. (2002) as the intrinsic quasar template spectrum. The O13 model has six free parameters: two for the quasar SED (tilt and normalization), two for the Lyman series opacity (γ_τ and $\tau_{\rm eff}^{\rm Ly}(\lambda_{912})$), and two to model the Lyman limit opacity (γ_κ and $\kappa_{912}^{\rm LL}(z_{\rm qso})$); ours has only two (the slope of the intrinsic SED, a, and $\kappa_{912}^{\rm LL}(z_{\rm qso})$).

We have thus refitted the O13 WFC3 quasar sample using our formalism to establish possible systematics among different assumptions. By assuming the intrinsic L15 quasar SED with no tilt, as this stack was constructed with the same data and we fit the spectra in the same wavelength interval as the one adopted by O13 (i.e., 700–911.76 Å), we find $\lambda_{\rm mfp}^{912} \simeq 213.8 \pm 28.0\ h_{70}^{-1}$ Mpc and $a = 0.95 \pm 0.04$.

From this comparison, we could conclude that quasar pairs and single quasars seem to trace similar IGM distributions. Nonetheless, our sample covers a broad redshift range (see Figure 1), so the $\tau_{\rm eff}^{\rm Ly}$ function employed (see Section 5.1) may have a tendency to over(or under)estimate the correction for quasars at low (high) redshifts with respect to the mean redshift of the sample (i.e., $z \simeq 2.26$). We have thus performed the whole analysis by assuming the 700–911.76 Å wavelength

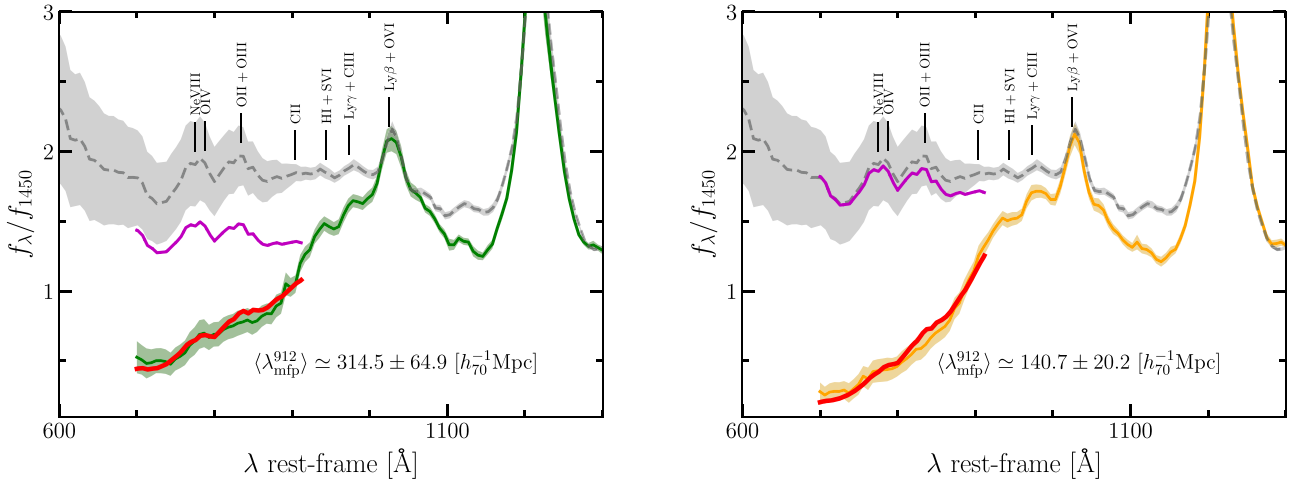

Figure 12. The green and orange solid lines are the observed WFC3 quasar pair composites for the low-z ($\langle z\rangle = 2.09$) and high-z ($\langle z\rangle = 2.44$) subsamples, respectively. Keys as in Figure 11.

range, the tilted L15 SED, and the $\tau_{\rm eff}^{\rm Ly}$ function relative to the low- and high-z samples at the average redshifts of $z \simeq 2.09$ and $z \simeq 2.44$, respectively. The resulting mean $\lambda_{\rm mfp}^{912}$ values are $\lambda_{\rm mfp}^{912} \simeq 315 \pm 65\ h_{70}^{-1}$ Mpc and $\lambda_{\rm mfp}^{912} \simeq 140 \pm 20\ h_{70}^{-1}$ Mpc for the low- and high-z samples, respectively, and the best-fit models are presented in Figure 12.

The difference between the $\lambda_{\rm mfp}^{912}$ value of O13 and the one we measured for the high-z quasar pair subsample is at the 2σ level. Despite the large uncertainties, our analysis of the $\lambda_{\rm mfp}^{912}$ suggests a possible difference in the environment of pairs with respect to single quasars at similar redshifts, in line with the comparisons of the observed UV stacks we have discussed in previous sections.

5.4. Redshift Evolution of the Mean Free Path

The evolution of the mean free path as a function of redshift provides insights on the cosmological distribution of gas around galaxies that dominates the hydrogen Lyman limit opacity. The most comprehensive collection of direct $\lambda_{\rm mfp}^{912}$ measurements is provided by Worseck et al. (2014, W14 hereafter, see their Table 4; see also Rudie et al. 2013). They found that $\lambda_{\rm mfp}^{912}$ increases by an order of magnitude from $z = 5$ to 2.5, where most of the measurements are at $z > 3$ and only two $\lambda_{\rm mfp}^{912}$ values are currently being estimated at $z = 2.0$–2.5. Our survey adds two additional data points on the $\lambda_{\rm mfp}^{912}$–z relation at $z < 3$ and allows us to directly compare the distribution of H I LL absorbers of quasar pairs with that of single quasars.

Figure 13 shows the mean free path to ionizing photons as a function of redshift with our additional measurements at $z = 2.0$–2.5. For a comparison, we overplot the complete set of $\lambda_{\rm mfp}^{912}$ estimates and their uncertainties published by W14. We overplot the best-fit function obtained by W14 to model the observed decrease of $\lambda_{\rm mfp}^{912}$ with increasing redshift: $A(1+z)^\eta$ with $\eta = -5.4 \pm 0.4$ and $A = 37 \pm 2\ h_{70}^{-1}$ Mpc. The red circle represents the best-fit value of $\lambda_{\rm mfp}^{912}$ obtained by applying our formalism to the O13 WFC3 sample, that is, $\lambda_{\rm mfp}^{912} \simeq 213.8 \pm 28.0\ h_{70}^{-1}$ Mpc, to be compared to $235.8 \pm 40.3\ h_{70}^{-1}$ Mpc obtained by W14 using the same data.

Overall, we find that our $\lambda_{\rm mfp}^{912}$ estimates are systematically lower with respect to the best-fit relation by W14 and that the

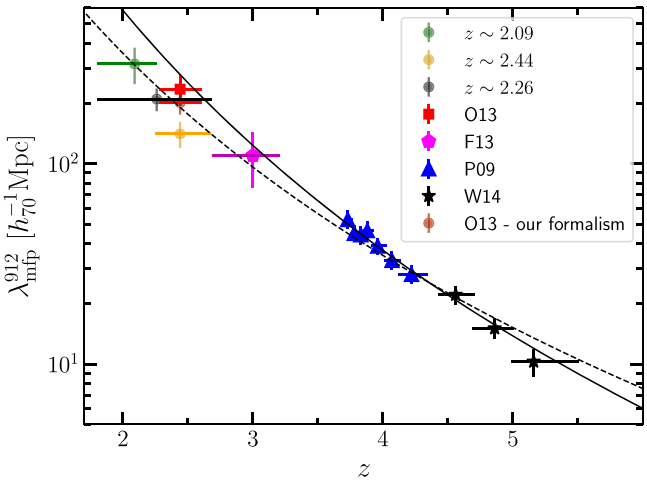

Figure 13. Mean free path to ionizing photons in the IGM as a function of redshift. The data points show the direct measurements of $\lambda_{\rm mfp}^{912}$ through the quasar spectral stacking analysis by Worseck et al. (2014, black stars), Prochaska et al. (2009, blue triangles), Fumagalli et al. (2013, magenta pentagon), and O13 (red square). The black solid circle represents the $\lambda_{\rm mfp}^{912}$ value estimated using the WFC3 quasar pair sample, while the red circle represents the best-fit $\lambda_{\rm mfp}^{912}$ value obtained by applying our formalism to the O13 WFC3 sample. The green and orange circles represent the mean $\lambda_{\rm mfp}^{912}$ obtained by splitting the WFC3 sample into low- and high-redshift bins. We also overplotted the best-fit function published by Worseck et al. (2014) to model the observed decrease of $\lambda_{\rm mfp}^{912}$ with increasing redshift: $(1+z)^\eta$ with $\eta \simeq -5.4$. The dashed line is the best fit obtained by also including the WFC3 low- and high-z $\lambda_{\rm mfp}^{912}$ values obtained with our analysis ($\eta \simeq -4.5 \pm 0.2$).

$\lambda_{\rm mfp}^{912}$ value of the high-redshift quasar pair sample is statistically different at the 2σ level with respect to the one for single quasars obtained by O13 when using the same fitting technique. By considering a two-parameter model in a fashion similar to the one adopted by W14, $\lambda_{\rm mfp}^{912}(z) = A[(1+z)/5]^\eta$, we find $\eta = -4.5 \pm 0.2$ and $A = 35.0 \pm 1.2\ h_{70}^{-1}$ Mpc (dashed line in Figure 13), which is different at the 2σ level with respect to the slope found by W14.

Estimates of the $\lambda_{\rm mfp}^{912}$ are very sensitive to the spectral shape at $\lambda < 910$ Å. Given that our WFC3 spectral composite displays a somewhat steeper slope at $\lambda < 912$ Å compared to the L15 one, our low $\lambda_{\rm mfp}^{912}$ values can be due to either a

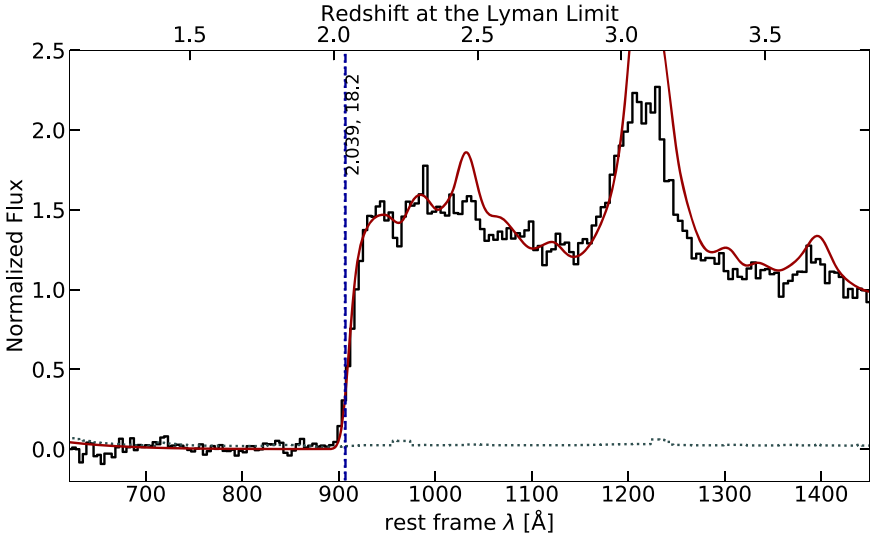

Figure 14. WFC3 quasar spectrum (black histogram) and the adopted model (red solid line) to identify the Lyman limit absorbers along the line of sight for SDSS J002424.21–012825.7. The dashed line reports the redshift of the quasar at the Lyman limit, while the dotted lines mark the redshift and the log $N_{\rm H\,I}$ for each LLS. (The complete figure set (94 images) is available.)

different evolution of the optically thick gas on cosmological scales, that is, changes in the gas accretion rate onto galactic halos at $z < 3$, or a different CGM/IGM distribution for pairs with respect to single quasars (i.e., a more dense or neutral environment for quasar pairs). We regard the first scenario unlikely, as a change in the relative contribution of optically thick absorbers to the mean free path would show as a break in the $\lambda_{\rm mfp}^{912}-z$ relation at $z < 3$ (Fumagalli et al. 2013). Yet, our data do not require a break in the power law presented in Figure 13. To explore the latter scenario, in the next section we analyze the WFC3 spectra together with the high-resolution ones (when available) to study the incidence of optically thick absorbers along the line of sight.

6. Fitting for LLS Absorbers

To further investigate whether the quasar pairs in our survey tend to live in a denser or more neutral environment than single quasars, we fit for absorbers by modeling each quasar spectrum using an approach similar to the one adopted by O13. We summarize the main steps. First, we need to estimate the level of continuum and the slope at $\lambda > 1200$ Å. For comparison purposes, we considered the same template as the one employed by O13, that is, a Telfer et al. (2002) quasar template spectrum, modulated by a scaled normalization and a tilt. The values of the normalization and the tilt have been determined utilizing a custom GUI that allows one to visually compare the quasar template for each WFC3 spectrum.[21] We then add one or more systems to model any drop in the observed flux at $\lambda < 912$ Å yielding significant opacity. To robustly identify absorption systems using low-resolution spectroscopy, spectral data with high S/N and quasars without complex ionizing continua are usually preferred. As our data set has relatively modest S/N, we also considered the additional SDSS data and the high-resolution spectroscopy from our ongoing follow-up campaign (at the time of writing, ∼50% of the sample has additional spectroscopy from ground-based facilities; see Section 2.3) to identify or confirm strong (log $N_{\rm H\,I} \geqslant 17.2$ or $\tau_{912}^{\rm LL} \geqslant 1$) absorbers through the presence of saturated H I absorption lines and narrow absorption line doublets such as C IV$\lambda\lambda$1548,1551. The analysis for each quasar spectrum was performed independently by E.L. and M. F., and then the models were visually inspected and compared. This exercise is meant to provide an indicative (but quantitative) estimate of the incidence of absorbers in our sample that we can then compare with the results from single quasars using similar data. A more in-depth analysis of the absorbers in our sample is not the purpose of this paper and will be presented in a forthcoming publication.

An example of this analysis is shown in Figure 14, where we present the final adopted model superimposed on the WFC3 spectrum (the redshifts of the identified absorbers are also displayed). As already discussed by O13, χ^2-minimization algorithms usually assign unrealistically small statistical errors (<2%), so we considered an uncertainty that is based on a comparison between the values for the redshift of the absorbers, $z_{\rm abs}$, and the column density obtained from the different authors. For systems with log $N_{\rm H\,I} > 17.2$, the uncertainty on $z_{\rm abs}$ is in the range ∼0.02–0.05 (≃1745–4400 km s^{-1}). Our survey is not complete for multiple absorbers with log $N_{\rm H\,I} < 17.2$ in the range 5000–10,000 km s^{-1} from the Lyman limit. Our main aim is, however, to identify strong LLSs and only use weak absorbers (log $N_{\rm H\,I} < 17.2$) to model the continuum.

When two absorbers are located within $|\delta v| < 10{,}000$ km s^{-1} ($\delta z \simeq 0.1$) and the redshifts are based on WFC3 spectra only (∼40% of the quasars in our sample), we tend to consider such complexes as a single LLS with a summed optical depth, similar to what is done in the O13 analysis. This choice overestimates the incidence of systems with $\tau_{912}^{\rm LL} \simeq 1$ by roughly 10% (see discussion in O13 and Prochaska et al. 2010), and it affects both quasar samples. Yet, while in our study we also based our identification on additional spectra with higher resolution data (e.g., ESI, Mage, BOSS, LIRIS) when available, the O13 analysis was based on WFC3 spectra only. Therefore, we may find more systems, especially at

[21] https://github.com/pyigm/pyigm

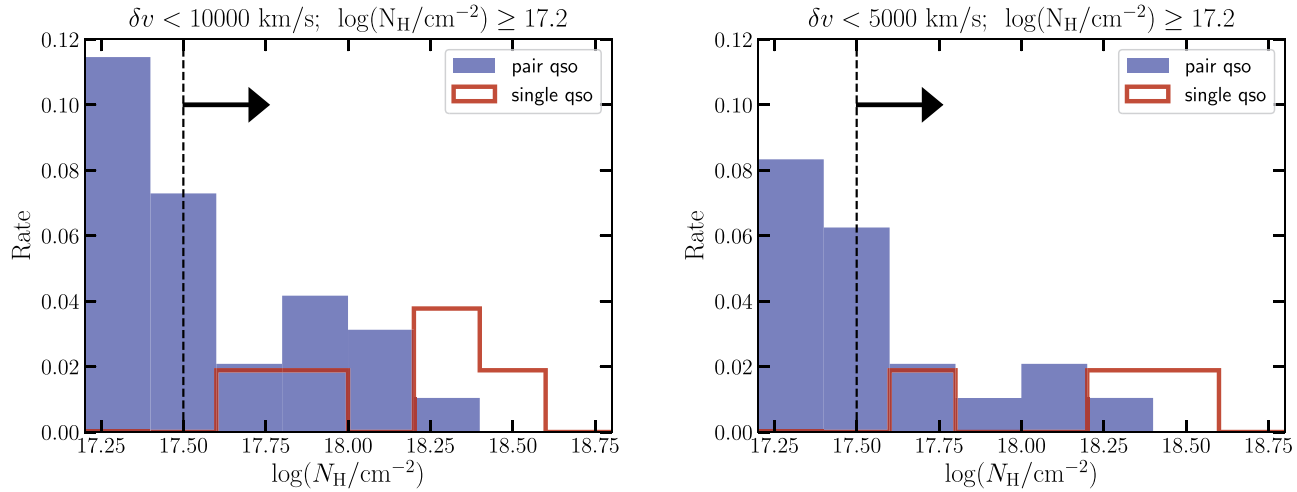

Figure 15. Absorber column density distribution for our quasar pair sample (blue shaded histogram) and the one by O13 of single quasars (red open histogram) for a velocity cut of $|\delta v| = 10{,}000$ km s^{-1} and $|\delta v| = 5000$ km s^{-1}, for the left and right panels, respectively. Each bin has been normalized to the total number of quasars in the two samples, that is, $N_{\rm TOT} = 94$ and 53 for our sample and the O13 one, respectively. All $N_{\rm H\,I}$ values higher than $10^{17.5}$ cm^{-2} should be considered lower limits.

$\log N_{\rm H\,I} \simeq 17.2$ or lower with respect to O13. As this may introduce biases in our comparison, we believe that considering only those absorbers with $\log N_{\rm H\,I} \geqslant 17.2$ at $|\delta v| < 5000$ km s^{-1} is a conservative choice that minimizes possible systematics.

During our search, we identified 28 (20) systems having $\log N_{\rm H\,I} \geqslant 17.2$ with $|\delta v| = 10{,}000$ km s^{-1} (5000 km s^{-1}), 14 (nine) of which with $\log N_{\rm H\,I} \geqslant 17.5$ and $|\delta v| = 10{,}000$ km s^{-1} (5000 km s^{-1}). Figure 15 presents the $N_{\rm H\,I}$ distributions of the absorbers for $|\delta v| < 5000$ and 10,000 km s^{-1} for our WFC3 quasar pair sample and for the O13 sample of single quasars, where they identified 109 absorbers overall (see their Table 2). The bins have been normalized to the total number of quasars in each sample (i.e., 53 sources for O13 and 94 in our analysis). Six percent of the O13 total quasar sample have $\log N_{\rm H\,I} \geqslant 17.2$ within $|\delta v| = 5000$ km s^{-1} (three absorbers), which is roughly a factor of three lower compared to our 20% (20 absorbers). If we assume an uncertainty on the identification of ± 2 in both samples (as we cannot resolve multiple strong absorbers within 10,000 km s^{-1}; see also Section 4.1 in O13), these two rates are different at the 5σ level. This result further suggests that the quasar pairs at 10–150 kpc (projected) separation observed in our survey tend to live in environments with denser or more neutral gas than single quasars, in line with the results of our mean free path analysis.

7. Discussion and Conclusion

In this study we characterize the spectral shape and environmental properties of close ($R_\perp \leqslant 150$ kpc) quasar pairs at $z = 2.0$–2.5, and we compare the results to studies of single quasars at similar redshifts. Below we summarize our main findings:

1. Our quasar pair sample leads to an ionizing power-law index of $\alpha_{\rm ion} \simeq -2.5 \pm 0.8$ (see Section 4.1), which, taken at face value, is softer (i.e., steeper) than the one obtained by L15 for single, much brighter quasars ($\alpha_{\rm ion} = -1.7 \pm 0.6$), although both are characterized by high uncertainties. This result assumes that the IGM distribution for the pair quasar sample is the same as that of single quasars at a similar redshift range. As our WFC3 quasar pair sample spans a broad redshift range, the assumption of an average IGM absorption function at the mean redshift of the sample may over(under)estimate the correction for quasars at low (high) redshifts with respect to the mean redshift of the sample (i.e., $z \simeq 2.26$). To check this point, we analyzed the quasar pair sample in two redshift bins.
2. When we create two composite samples binned by redshift, we find that the high-redshift quasar pair composite ($\langle z \rangle \simeq 2.44$) shows a factor of about two lower fluxes at rest wavelengths below ~900 Å compared to the L15 one, which considers quasars at the same average redshift. On the other hand, the level of absorption of the pair composite in the low-redshift interval ($\langle z \rangle \simeq 2.09$) is overall similar to the L15 stack (see Figure 5). We thus conclude that our assumption of a similar IGM distribution for the two samples at similar average redshift is likely incorrect and uncovers differences in the gas distribution between pairs and single quasars.
3. We find lower values of $\lambda_{\rm mfp}^{912}$ for pairs ($\lambda_{\rm mfp}^{912} \simeq 140.7 \pm 20.2\,h_{70}^{-1}$ Mpc) compared to single quasars ($\lambda_{\rm mfp}^{912} \simeq 213.8 \pm 28\,h_{70}^{-1}$ Mpc) at similar redshifts. Yet, uncertainties are large given the current data (the difference is at the 2σ level). As a result of our $\lambda_{\rm mfp}^{912}$ analysis and its evolution with time, we cannot rule out a difference in the relative contribution of absorbers (DLAs, LLSs) along the line of sight.
4. When we search the spectra for strong absorbers, we find that 6% of the O13 total quasar sample have absorbers with $\log N_{\rm H\,I} \geqslant 17.2$ within $|\delta v| = 5000$ km s^{-1} (three absorbers), which is roughly a factor of three lower compared to our 20% (20 absorbers). These two rates are significantly different at the 5σ level.

7.1. Implication for the Quasar Environment

Studies of quasar environments at various scales (from a few kiloparsecs to megaparsecs) and at different cosmic epochs are fundamental to understanding the role of the large-scale

environment in driving matter into the center of galaxies, possibly triggering the quasar activity. One way to investigate a quasar's environment is to measure the incidence of strong H I absorbers in quasar sight lines, which trace the distribution of cool, dense gas that forms structures.

In the case of a single quasar, the expectation for the incidence of Lyman limit absorption systems per unit path length (i.e., the number density of LLSs per unit redshift), $N(z)$, is $\simeq 0.96^{+0.23}_{-0.29}$ at $z \simeq 2.2$ (O'Meara et al. 2013, see their Figure 5 and Table 5). In other words, a quasar will hit on average roughly one absorber within a path $\Delta z = 1$ along the line of sight (see also Shull et al. 2017 for similar results at $z < 0.5$). As absorbers along the line of sight are often found to be intervening, optically thick absorbers tend to be located at relatively large distances from luminous quasars and not in close proximity to the quasars themselves. This effect can be attributed to the elevated radiation field near quasars. Indeed, Hennawi et al. (2006a) argued that for a quasar at $z = 2.5$ with an r-band magnitude of $r = 19$, the continuum ionizing flux is 130 times higher than that of the extragalactic UV background at an angular separation of 60″, which corresponds to a proper distance of $340\,h^{-1}$ kpc (see also Hennawi & Prochaska 2007). This enhanced ionization of clouds near the quasar gives rise to the *proximity effect* (Bajtlik et al. 1988).

The effects of ionization, however, are expected to be nonisotropic due to quasar beaming. Indeed, Hennawi et al. (2006a) presented a technique for studying the clustering of absorbers near luminous quasars in the transverse direction, perpendicular to the direction in which the quasar is radiating. To this end, they made use of alignments of background quasar sight lines to search for optically thick absorption in the vicinity of foreground quasars at $1.9 < z_{\rm fg} < 4.0$, finding a high incidence of optically thick gas in the circumgalactic medium of the quasar host, much in excess of observations along the line of sight. This result provides significant evidence that these absorbers are, indeed, strongly clustered around quasars (see also Hennawi et al. 2006b, 2010; Hennawi & Prochaska 2007), but likely photoionized along the line of sight. By using a background quasar sight line to study the foreground quasar's environment in absorption (where the pairs are thus at different redshift), Prochaska et al. (2013) also found an excess of H I Lyα absorption in the $30\,{\rm kpc} < R_\perp \leqslant 1\,{\rm Mpc}$ environment transverse of 650 projected quasar pairs at $z \sim 2$. In agreement with previous studies, their analysis is consistent with quasars being hosted by massive dark matter halos $M_{\rm halo} \simeq 10^{12.5} M_\odot$ at $z \sim 2.5$, where the transverse direction is much less likely to be illuminated by ionizing radiation than the line of sight (see also White et al. 2012).

The synergy between these two effects (quasar photoionization versus excess of H I absorption surrounding the quasars) is complex and depends upon many factors, such as the mass of the host galaxy (i.e., the mass of the halo) and the luminosity and opening angle of the quasar (e.g., Faucher-Giguère et al. 2008). The case of closely separated quasar pairs ($R_\perp \leqslant 150$ kpc) at similar redshifts ($\Delta z \leqslant 10$ Mpc, Figure 3) is thus of particular interest as, different from projected pairs, these systems are excellent tracers of the environment of quasars that share the same large-scale structure, or in some cases even the same dark matter halos.

Our WFC3 pair sample shows an enhancement of LLSs with $\log N_{\rm H\,I} \simeq 17.2$ at $|\delta v| < 5000\,{\rm km\,s^{-1}}$ compared to single quasars at the 5σ level along the line of sight. This higher incidence of optically thick gas along the pairs' sight lines explains the softer shape of the composite quasar pair stack when compared to that of single quasars at similar redshift (see left panels of Figures 4 and 5). Among the 20 strong absorbers we found, six of them lie in correlated pairs (all in the low-redshift bin), while the rest are equally shared between the low- and high-redshift bins (see Figure 3). Moreover, we find that the location of these 20 absorbers is equally shared between foreground and background quasars, with nine absorbers identified in background quasars and 11 absorbers in foreground sources. We still retrieve an equal fraction of strong absorbers in the foreground and background quasar if we consider absorbers at $|\delta v| < 3000\,{\rm km\,s^{-1}}$ (14 absorbers). There is no obvious trend with magnitudes, as these 20 absorbers are located in quasars having average r^* magnitudes typical of the overall sample ($r^* \simeq 20$).

Despite the small statistics, this implies that both foreground and background quasars are embedded in the same, and equally dense and (partially) neutral, environment at <15 Mpc (Figure 3). This is different from what is seen in single quasars, and also from the results of the projected pairs, where the background sight lines show a clear excess of absorbers at the redshift of the foreground quasars. Given that the mean luminosity is about a factor of three fainter than the typical quasars considered by Hennawi et al. (2006a), we argue that the higher fraction of optically thick absorbers in quasar pairs is not primarily driven by a lower radiation field. Instead, based on this analysis, we argue that the gas-absorbing Lyman limit photons in our WFC3 sample of closely projected quasar pairs is likely to arise mostly within structures located in denser regions within the CGM or IGM where both quasars reside.

We are grateful to the referee, Prof. Michael Shull, for his thorough reading and for useful comments and suggestions that have significantly improved the clarity of the paper. E.L. thanks G. Calderone for having modified the code QSFit to handle low-resolution WFC3 spectra and for feedback and suggestions on the fitting procedure. E.L. is supported by a European Union COFUND/Durham Junior Research Fellowship (under EU grant agreement 609412). M.F. acknowledges support by the Science and Technology Facilities Council (grant ST/P000541/1). This project has received funding from the European Research Council (ERC) under the European Union's Horizon 2020 research and innovation program (grant agreement 757535). Support for HST Program GO-14127 was provided by NASA through grants from the Space Telescope Science Institute, which is operated by the Association of Universities for Research in Astronomy, Inc., under NASA contract NAS526555. M.R. acknowledges support by HST-GO-14127.011 and a NASA Keck PI Data Award, administered by the NASA Exoplanet Science Institute. Some of the data presented herein were obtained at the W.M. Keck Observatory from telescope time allocated to the National Aeronautics and Space Administration through the agency's scientific partnership with the California Institute of Technology and the University of California. The Observatory was made possible by the generous financial support of the W.M. Keck Foundation. The authors wish to recognize and acknowledge the very significant cultural role and reverence that the summit of Maunakea has always had within the indigenous Hawaiian community. We are most fortunate to have the opportunity to conduct observations from this mountain.

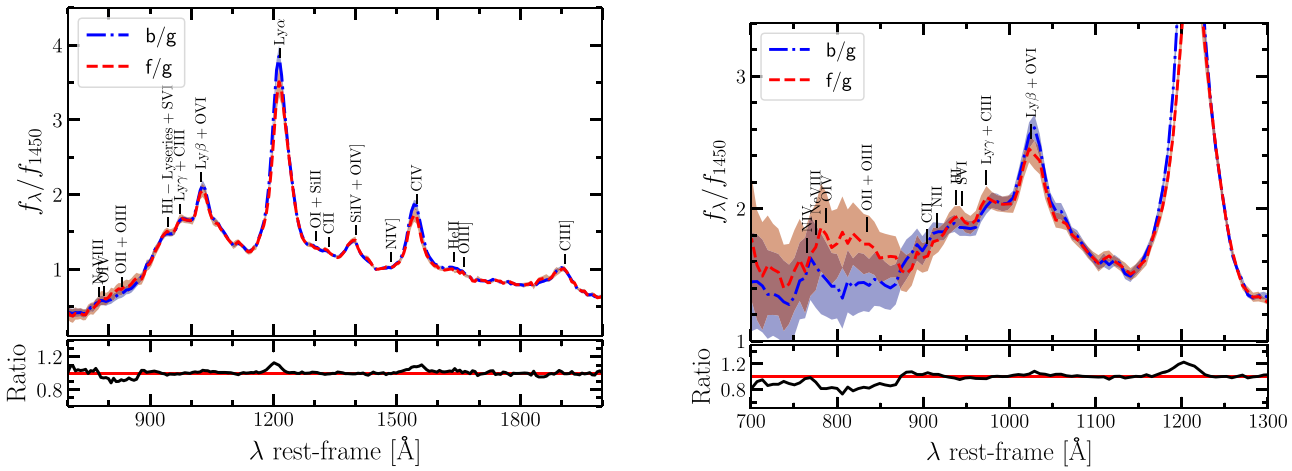

Figure 16. Left panel: mean observed quasar spectrum (from bootstrap) for the background quasars (blue dot-dashed line) compared to the one obtained for the foreground quasars (red dashed line). The background-to-foreground spectral ratio is shown in the bottom panel. Right panel: mean IGM-corrected quasar spectrum with uncertainties from bootstrap (shaded area) for the background quasars (blue dot-dashed line) compared to the one obtained for the foreground quasars (red dashed line).

Facilities: HST (WFC3), Keck:II (ESI).

Software: astropy (Astropy Collaboration et al. 2013), corner (Foreman-Mackey 2016), matplotlib (Hunter 2007), emcee (Foreman-Mackey et al. 2013), QSFit (Calderone et al. 2017).

Appendix
Comparison of Foreground and Background Spectral Stacks

In Figure 16 we present the mean observed and corrected for IGM absorption composite normalized to unity at 1450 Å for the background (mean/median redshift is 2.275/2.249) and foreground (mean/median redshift is 2.255/2.236) quasar samples separately. It is clear from this comparison that both samples have very similar ionizing continua, while differences arise in the most prominent broad emission lines (C IV and Lyα), in the form of a ∼20%–25% emission line flux increase for the background quasar stack compared to the foreground one. Such a feature is likely due to a mild Baldwin effect as the foreground quasars are, on average, somewhat brighter (mean/median $g^* = 20.10/20.24$) than the background (mean/median $g^* = 20.21/20.35$) sources.

Moreover, a ∼20% flux decrement at $\lambda \simeq 760$–880 Å in the background composite with respect to the foreground one is also present, falling in the midst of prominent quasar emission lines (i.e., Ne VIII$\lambda\lambda$775, O IVλ788, O II+O III$\lambda\lambda$834.5). We note that this is not highly significant as uncertainties on the average spectra are of the order of ∼10%–12% at $\lambda \simeq 800$ Å. We should also point out that our estimates of the quasar redshifts can be fairly uncertain ($\sigma_z \sim 500$–1000 km s^{-1}), as they have been evaluated from C IV for the majority of the sources in the sample (thus subject to offsets from the systemic; e.g., 500–1000 km s^{-1}; Corbin 1990), while only a few cases (Mg II, $\sigma_z \sim 200$–500 km s^{-1}) were available.[22] Given that the pair separations are very small, it is then possible to confuse a background with a foreground pair, and vice versa.

[22] Corbin (1990) found that the velocity difference between the Mg II and C IV lines could exceed 4000 km s^{-1}, while the one of C IV from C III] exceeds 2000 km s^{-1}.

ORCID iDs

Elisabeta Lusso https://orcid.org/0000-0003-0083-1157
Michele Fumagalli https://orcid.org/0000-0001-6676-3842
Marc Rafelski https://orcid.org/0000-0002-9946-4731
Jason X. Prochaska https://orcid.org/0000-0002-7738-6875
Joseph F. Hennawi https://orcid.org/0000-0002-7054-4332
John M. O'Meara https://orcid.org/0000-0002-7893-1054

References

Alexander, D. M., & Hickox, R. C. 2012, NewAR, 56, 93
Anderson, J., & Bedin, L. R. 2010, PASP, 122, 1035
Anguita, T., Faure, C., Yonehara, A., et al. 2008, A&A, 481, 615
Astropy Collaboration, Robitaille, T. P., Tollerud, E. J., et al. 2013, A&A, 558, A33
Bajtlik, S., Duncan, R. C., & Ostriker, J. P. 1988, ApJ, 327, 570
Baldwin, J. A. 1977, ApJ, 214, 679
Bershady, M. A., Charlton, J. C., & Geoffroy, J. M. 1999, ApJ, 518, 103
Brotherton, M. S., Tran, H. D., Becker, R. H., et al. 2001, ApJ, 546, 775
Calderone, G., Nicastro, L., Ghisellini, G., et al. 2017, MNRAS, 472, 4051
Cisternas, M., Jahnke, K., Inskip, K. J., et al. 2011, ApJ, 726, 57
Claeskens, J.-F., Surdej, J., & Remy, M. 1996, A&A, 305, L9
Compostella, M., Cantalupo, S., & Porciani, C. 2013, MNRAS, 435, 3169
Corbin, M. R. 1990, ApJ, 357, 346
Corbin, M. R. 2000, ApJL, 536, L73
Czerny, B., & Elvis, M. 1987, ApJ, 321, 305
Danforth, C. W., Keeney, B. A., Tilton, E. M., et al. 2016, ApJ, 817, 111
Deane, R. P., Paragi, Z., Jarvis, M. J., et al. 2014, Natur, 511, 57
Dietrich, M., Hamann, F., Shields, J. C., et al. 2002, ApJ, 581, 912
Di Matteo, T., Springel, V., & Hernquist, L. 2005, Natur, 433, 604
Djorgovski, S. G., Courbin, F., Meylan, G., et al. 2007, ApJL, 662, L1
Eftekharzadeh, S., Myers, A. D., Hennawi, J. F., et al. 2017, MNRAS, 468, 77
Espey, B. R., Carswell, R. F., Bailey, J. A., Smith, M. G., & Ward, M. J. 1989, ApJ, 342, 666
Fardal, M. A., Giroux, M. L., & Shull, J. M. 1998, AJ, 115, 2206
Farina, E. P., Montuori, C., Decarli, R., & Fumagalli, M. 2013, MNRAS, 431, 1019
Faucher-Giguère, C.-A., Lidz, A., Hernquist, L., & Zaldarriaga, M. 2008, ApJ, 688, 85
Faucher-Giguère, C.-A., Lidz, A., Zaldarriaga, M., & Hernquist, L. 2009, ApJ, 703, 1416
Findlay, J. R., Prochaska, J. X., Hennawi, J. F., et al. 2018, arXiv: 1804.08624
Fitzpatrick, E. L. 1999, PASP, 111, 63
Fontanot, F., Cristiani, S., Pfrommer, C., Cupani, G., & Vanzella, E. 2014, MNRAS, 438, 2097
Fontanot, F., Cristiani, S., & Vanzella, E. 2012, MNRAS, 425, 1413
Foreman, G., Volonteri, M., & Dotti, M. 2009, ApJ, 693, 1554
Foreman-Mackey, D. 2016, JOSS, 1, 24

Foreman-Mackey, D., Hogg, D. W., Lang, D., & Goodman, J. 2013, PASP, 125, 306
Francis, P. J., Hewett, P. C., Foltz, C. B., et al. 1991, ApJ, 373, 465
Fumagalli, M., Hennawi, J. F., Prochaska, J. X., et al. 2014, ApJ, 780, 74
Fumagalli, M., O'Meara, J. M., Prochaska, J. X., & Worseck, G. 2013, ApJ, 775, 78
Furlanetto, S. R. 2009, ApJ, 703, 702
Gaskell, C. M. 1982, ApJ, 263, 79
Green, P. J. 1996, ApJ, 467, 61
Haardt, F., & Madau, P. 1996, ApJ, 461, 20
Haardt, F., & Madau, P. 2012, ApJ, 746, 125
Hennawi, J. F., Myers, A. D., Shen, Y., et al. 2010, ApJ, 719, 1672
Hennawi, J. F., & Prochaska, J. X. 2007, ApJ, 655, 735
Hennawi, J. F., Prochaska, J. X., Burles, S., et al. 2006a, ApJ, 651, 61
Hennawi, J. F., Prochaska, J. X., Cantalupo, S., & Arrigoni-Battaia, F. 2015, Sci, 348, 779
Hennawi, J. F., Strauss, M. A., Oguri, M., et al. 2006b, AJ, 131, 1
Hopkins, P. F., Hernquist, L., Cox, T. J., et al. 2005, ApJ, 630, 705
Hopkins, P. F., Hernquist, L., Cox, T. J., et al. 2006, ApJS, 163, 1
Hopkins, P. F., Hernquist, L., Cox, T. J., & Kereš, D. 2008, ApJS, 175, 356
Hunter, J. D. 2007, CSE, 9, 90
Inoue, A. K., & Iwata, I. 2008, MNRAS, 387, 1681
Inoue, A. K., Shimizu, I., Iwata, I., & Tanaka, M. 2014, MNRAS, 442, 1805
Jiang, L., Fan, X., Annis, J., et al. 2008, AJ, 135, 1057
Laor, A., Fiore, F., Elvis, M., Wilkes, B. J., & McDowell, J. C. 1997, ApJ, 477, 93
Liu, X., Shen, Y., & Strauss, M. A. 2011, ApJL, 736, L7
Lusso, E., Worseck, G., Hennawi, J. F., et al. 2015, MNRAS, 449, 4204
MacLeod, C. L., Ivezić, Ž., Sesar, B., et al. 2012, ApJ, 753, 106
Madau, P. 1995, ApJ, 441, 18
Madau, P., & Haardt, F. 2015, ApJL, 813, L8
Madau, P., Haardt, F., & Rees, M. J. 1999, ApJ, 514, 648
Malkan, M. A., & Sargent, W. L. W. 1982, ApJ, 254, 22
Massey, R., Stoughton, C., Leauthaud, A., et al. 2010, MNRAS, 401, 371
McQuinn, M., Lidz, A., Zaldarriaga, M., et al. 2009, ApJ, 694, 842
Meiksin, A. 2005, MNRAS, 356, 596
Meiksin, A. 2006, MNRAS, 365, 807
Meiksin, A., & White, M. 2003, MNRAS, 342, 1205
Miralda-Escudé, J., Haehnelt, M., & Rees, M. J. 2000, ApJ, 530, 1
Moller, P., & Jakobsen, P. 1990, A&A, 228, 299
Myers, A. D., Richards, G. T., Brunner, R. J., et al. 2008, ApJ, 678, 635
Netzer, H., Laor, A., & Gondhalekar, P. M. 1992, MNRAS, 254, 15
O'Meara, J. M., Prochaska, J. X., Chen, H.-W., & Madau, P. 2011, ApJS, 195, 16
O'Meara, J. M., Prochaska, J. X., Worseck, G., Chen, H.-W., & Madau, P. 2013, ApJ, 765, 137
Prochaska, J. X., Hennawi, J. F., Lee, K.-G., et al. 2013, ApJ, 776, 136
Prochaska, J. X., Madau, P., O'Meara, J. M., & Fumagalli, M. 2014, MNRAS, 438, 476
Prochaska, J. X., O'Meara, J. M., & Worseck, G. 2010, ApJ, 718, 392
Prochaska, J. X., Worseck, G., & O'Meara, J. M. 2009, ApJL, 705, L113
Rafelski, M., Teplitz, H. I., Gardner, J. P., et al. 2015, AJ, 150, 31
Rauch, M., Miralda-Escudé, J., Sargent, W. L. W., et al. 1997, ApJ, 489, 7
Ribaudo, J., Lehner, N., & Howk, J. C. 2011, ApJ, 736, 42
Richards, G. T., Vanden Berk, D. E., Reichard, T. A., et al. 2002, AJ, 124, 1
Richards, G. T., Strauss, M. A., Fan, X., et al. 2006, AJ, 131, 2766
Rudie, G. C., Steidel, C. C., Shapley, A. E., & Pettini, M. 2013, ApJ, 769, 146
Sandrinelli, A., Falomo, R., Treves, A., Farina, E. P., & Uslenghi, M. 2014, MNRAS, 444, 1835
Sandrinelli, A., Falomo, R., Treves, A., Scarpa, R., & Uslenghi, M. 2018, MNRAS, 474, 4925
Satyapal, S., Ellison, S. L., McAlpine, W., et al. 2014, MNRAS, 441, 1297
Satyapal, S., Secrest, N. J., Ricci, C., et al. 2017, ApJ, 848, 126
Schlafly, E. F., & Finkbeiner, D. P. 2011, ApJ, 737, 103
Scott, J. E., Kriss, G. A., Brotherton, M., et al. 2004, ApJ, 615, 135
Shankar, F., & Mathur, S. 2007, ApJ, 660, 1051
Shen, Y., Richards, G. T., Strauss, M. A., et al. 2011, ApJS, 194, 45
Shull, J. M., Danforth, C. W., Tilton, E. M., Moloney, J., & Stevans, M. L. 2017, ApJ, 849, 106
Shull, J. M., Roberts, D., Giroux, M. L., Penton, S. V., & Fardal, M. A. 1999, AJ, 118, 1450
Shull, J. M., Stevans, M., & Danforth, C. W. 2012, ApJ, 752, 162
Springel, V., Di Matteo, T., & Hernquist, L. 2005, MNRAS, 361, 776
Stevans, M. L., Shull, J. M., Danforth, C. W., & Tilton, E. M. 2014, ApJ, 794, 75
Surdej, J., Claeskens, J.-F., Remy, M., et al. 1997, A&A, 327, L1
Telfer, R. C., Zheng, W., Kriss, G. A., & Davidsen, A. F. 2002, ApJ, 565, 773
Tilton, E. M., Stevans, M. L., Shull, J. M., & Danforth, C. W. 2016, ApJ, 817, 56
Vanden Berk, D. E., Richards, G. T., Bauer, A., et al. 2001, AJ, 122, 549
Vasei, K., Siana, B., Shapley, A. E., et al. 2016, ApJ, 831, 38
Véron-Cetty, M.-P., Joly, M., & Véron, P. 2004, A&A, 417, 515
Vestergaard, M., & Wilkes, B. J. 2001, ApJS, 134, 1
Weston, M. E., McIntosh, D. H., Brodwin, M., et al. 2017, MNRAS, 464, 3882
White, M., Myers, Adam, D., Ross, N. P., et al. 2012, MNRAS, 424, 933
Willott, C. J., Delorme, P., Reylé, C., et al. 2010, AJ, 139, 906
Worseck, G., & Prochaska, J. X. 2011, ApJ, 728, 23
Worseck, G., Prochaska, J. X., O'Meara, J. M., et al. 2014, MNRAS, 445, 1745
Zheng, W., Kriss, G. A., Telfer, R. C., Grimes, J. P., & Davidsen, A. F. 1997, ApJ, 475, 469
Zheng, W., & Malkan, M. A. 1993, ApJ, 415, 517